ELECTRONIC SUPPORTING INFORMATION

Luminescent Er^{3+} Based Single Molecule Magnets with Fluorinated Alkoxide or Aryloxide Ligands

Alexander A. Selikhov,[a,b] Gautier Félix,[c] Dmitry M. Lyubov,[a,b] Yulia V. Nelyubina,[a,] Anton V. Cherkasov,[b] Saad Sene,[c] Ilya V. Taydakov,[d] Mikhail T. Metlin,[a] Andrey A. Tyutyunov,[a] Yannick Guari,[c] Joulia Larionova*[c] and Alexander A. Trifonov*[a,b]

[a] *A. N. Nesmeyanov Institute of Organoelement Compounds of Russian Academy of Sciences, 28 Vavilova str., 119334 , Moscow, Russia. E-mail: trif@iomc.ras.ru*

[b] *Institute of Organometallic Chemistry of Russian Academy of Sciences, 49 Tropinina str., GSP-445, 630950, Nizhny Novgorod, Russia. E-mail: trif@iomc.ras.ru*

[c] *ICGM, Univ. Montpellier, CNRS, ENSCM, Montpellier, France. E-mail: joulia.larionova@umontpellier.fr*

[d] *N. D. Zelinsky Institute of Organic Chemistry Russian Academy of Sciences, Leninsky Prospect, 47, 119991, Moscow, Russia*

TABLE OF CONTENTS

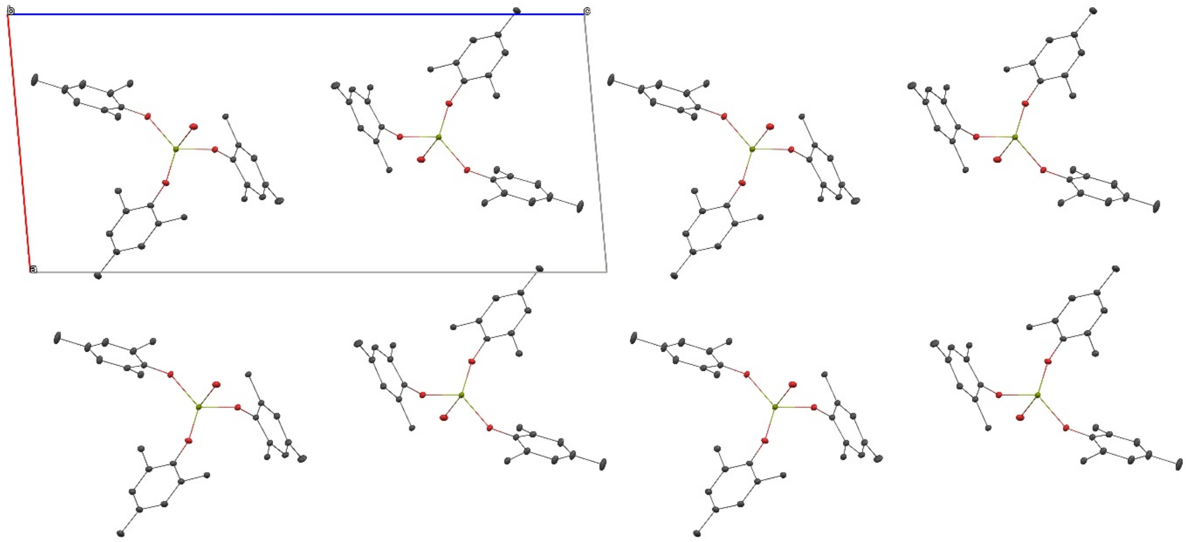

Figure S1. Perspective view of the crystal packing for **1** along the crystallographic axis *b*. Color code: light green Er; yellow F; red O; grey C. Hydrogen atoms and crystallized solvent molecules have been omitted for clarity.

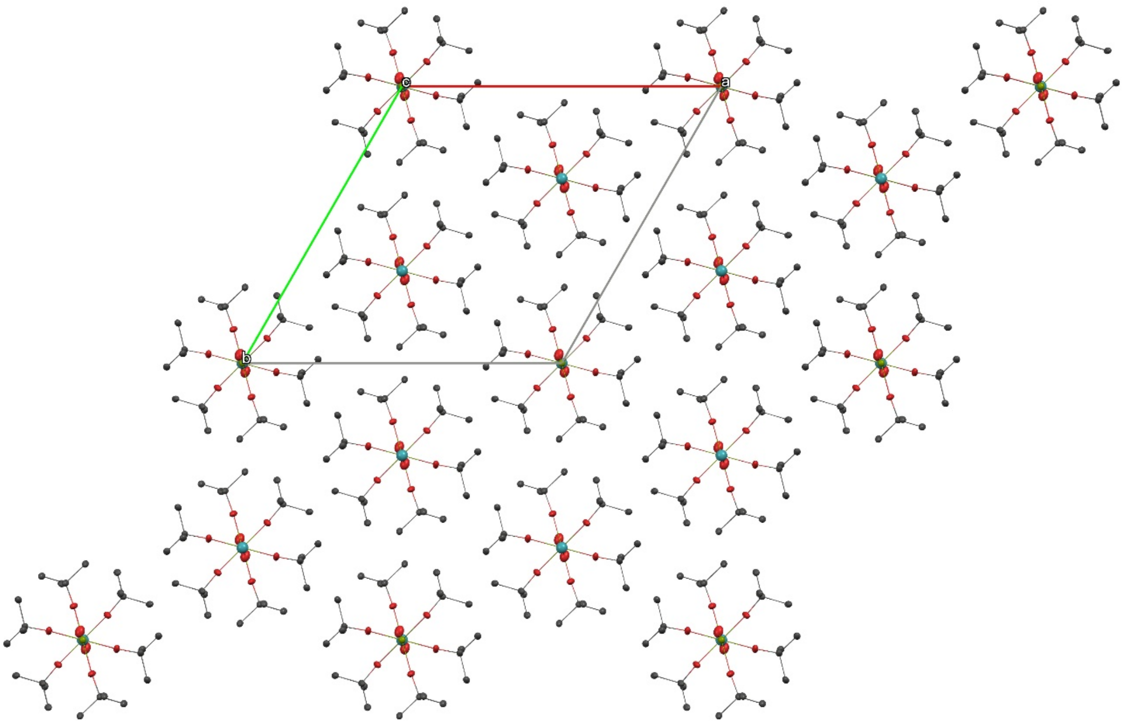

Figure S2. Perspective view of the crystal packing for **2** along the crystallographic axis *c*. Color code: light green Er; yellow F; red O; grey C. Hydrogen atoms and crystallized solvent molecules have been omitted for clarity.

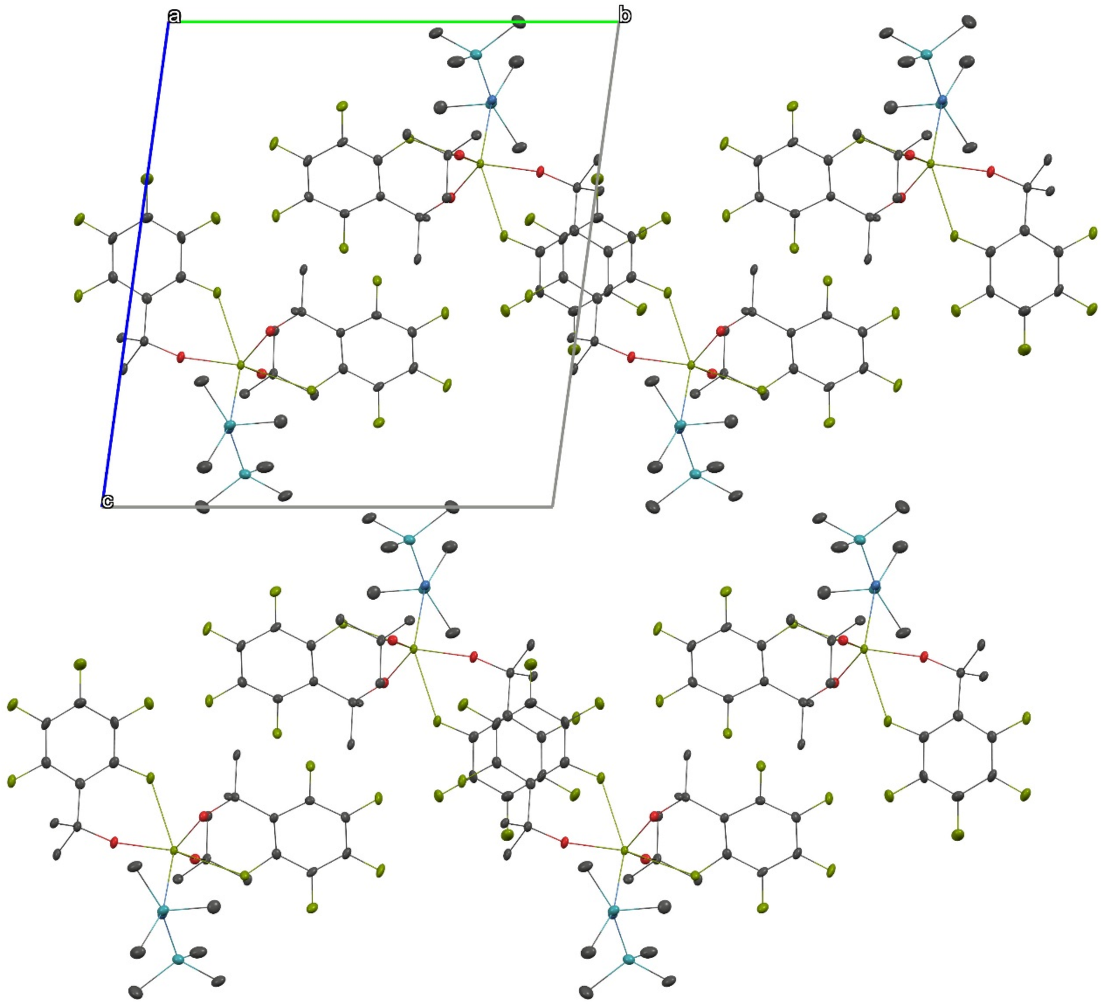

Figure S3. Perspective view of the crystal packing for **3** along the crystallographic axis *a.* Color code: light green Er; yellow F; red O; grey C. Hydrogen atoms and crystallized solvent molecules have been omitted for clarity.

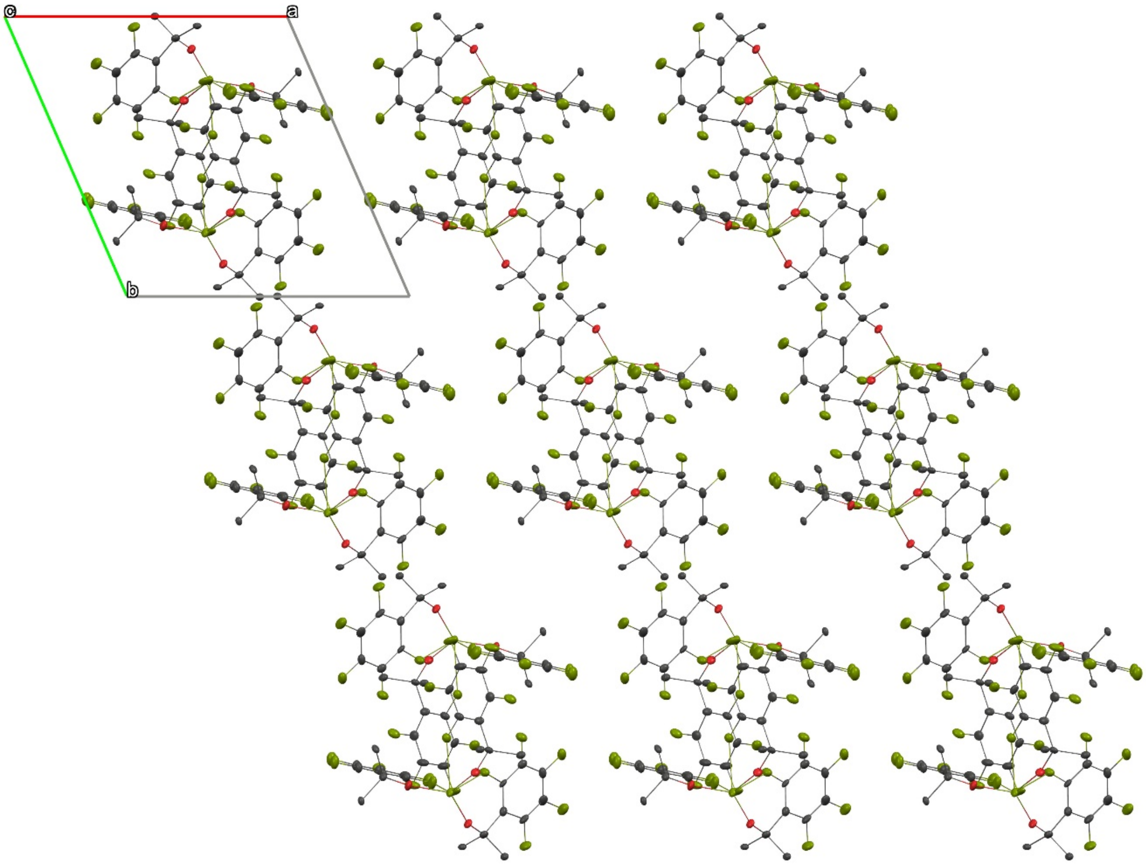

Figure S4. Perspective view of the crystal packing for **4** along the crystallographic axis *c*. Color code: light green Er; yellow F; red O; grey C. Hydrogen atoms and crystallized solvent molecules have been omitted for clarity.

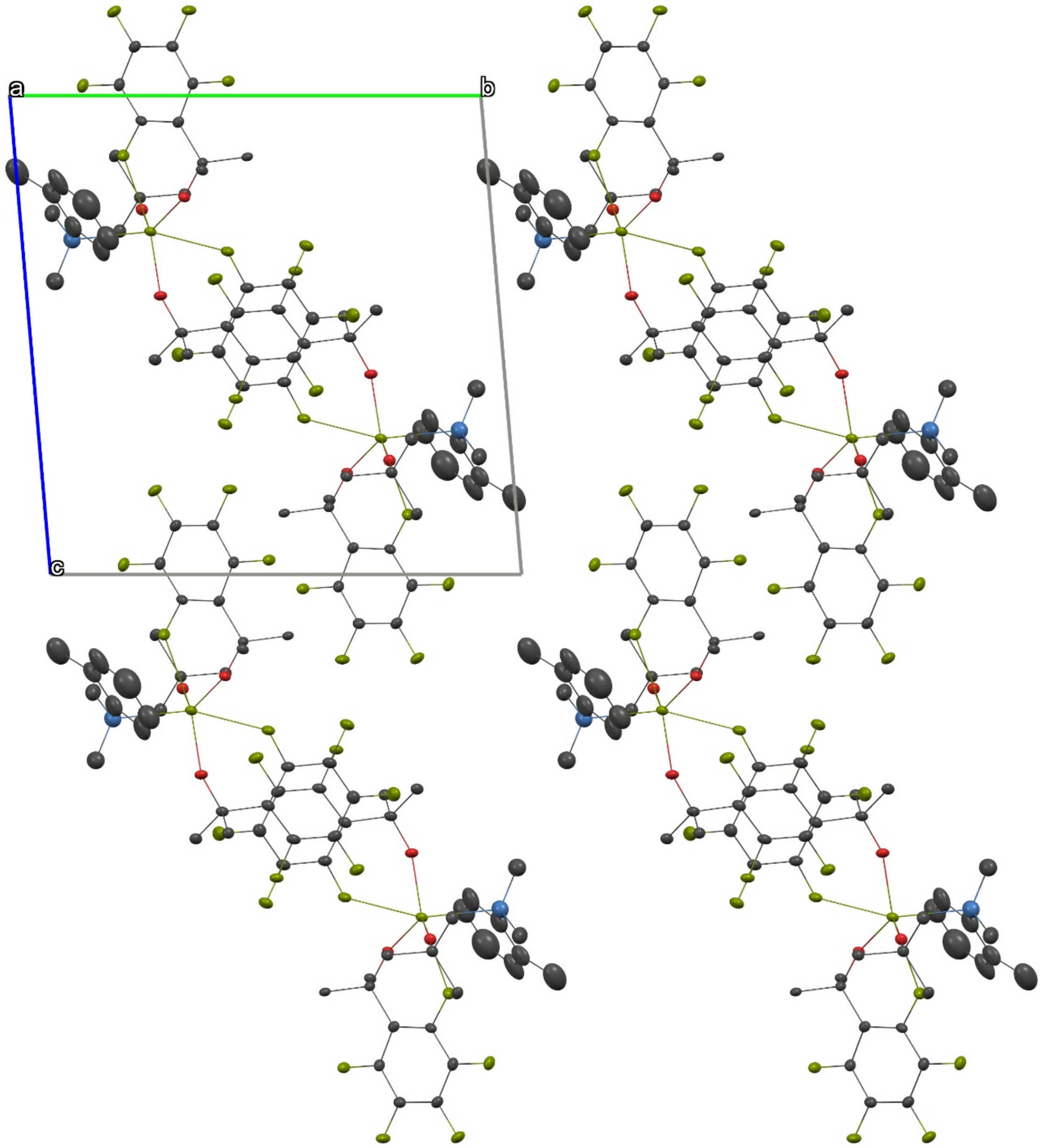

Figure S5. Perspective view of the crystal packing for **5** along the crystallographic axis *a*. Color code: light green Er; yellow F; red O; grey C. Hydrogen atoms and crystallized solvent molecules have been omitted for clarity.

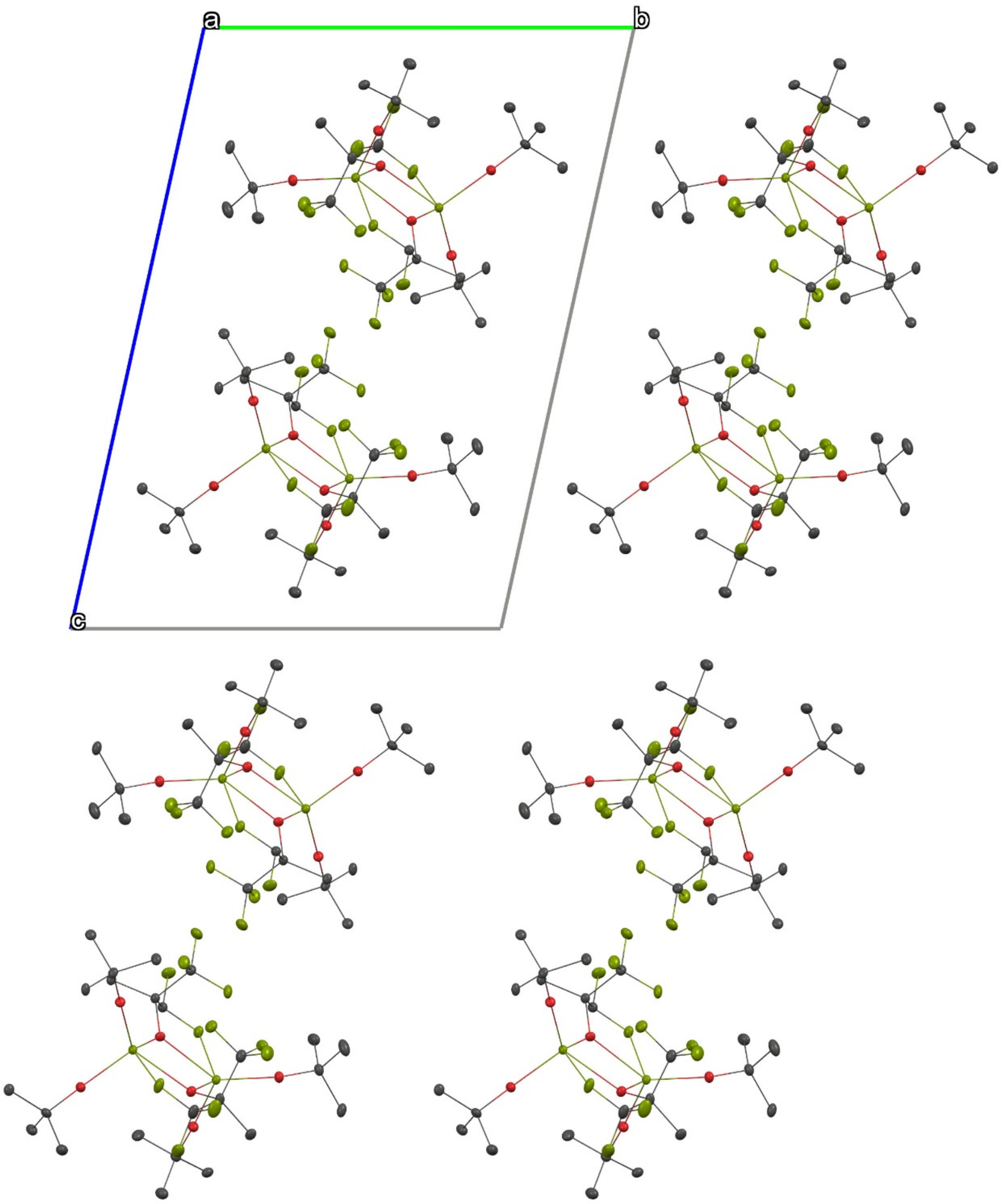

Figure S6. Perspective view of the crystal packing for **6** along the crystallographic axis *a*. Color code: light green Er; yellow F; red O; grey C. Hydrogen atoms and crystallized solvent molecules have been omitted for clarity.

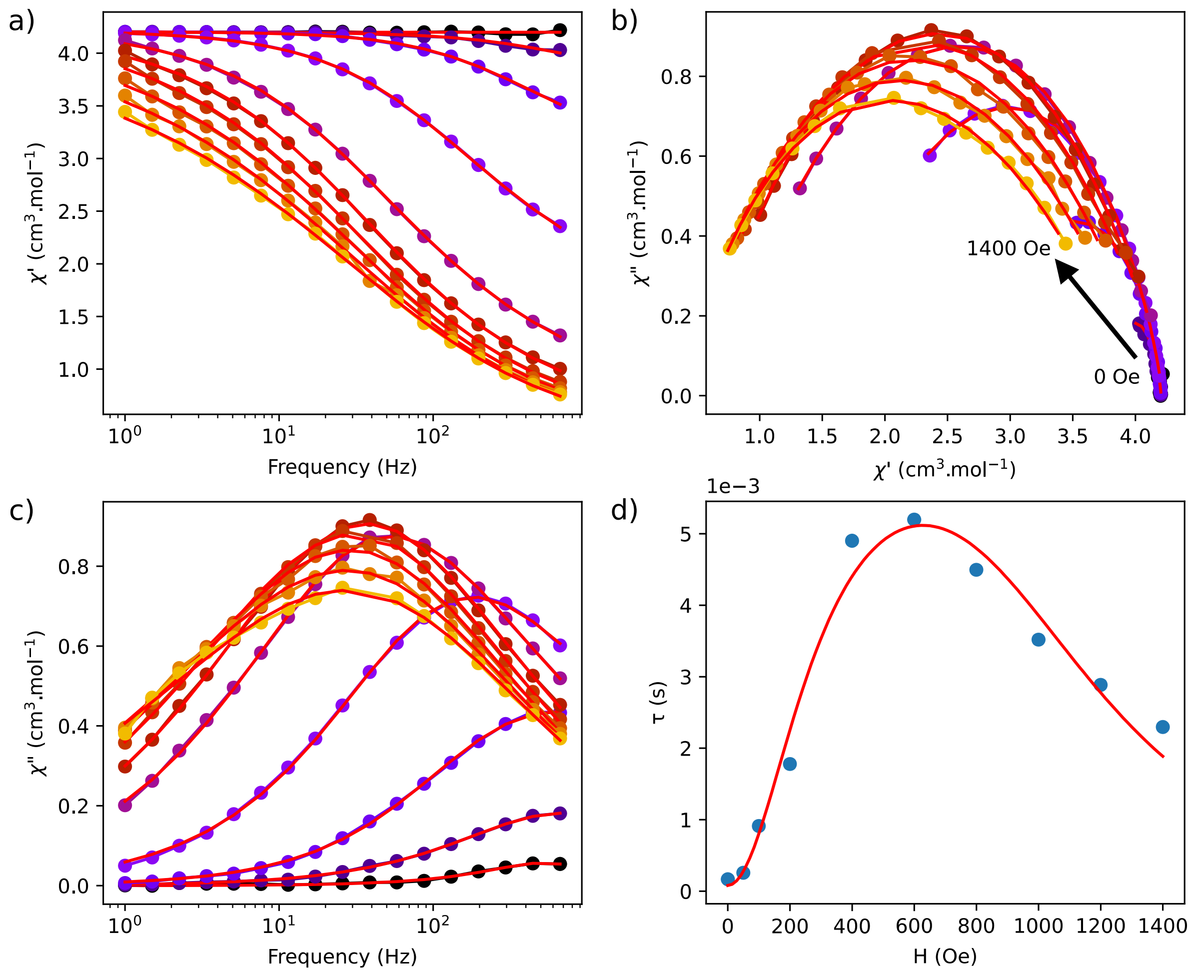

Figure S7. Frequency dependence of χ' (a) and χ'' (c) for **2** at 1.8 K performed under various applied dc fields. (b) Cole-Cole plots obtained using the frequency dependence of χ'' for **2** at 1.8 K under various dc field. The solid lines correspond to the best fit obtained with a generalized Debye model. (d) Field dependence of the relaxation time curve for **2**. The red line represents the fit using equation (1).

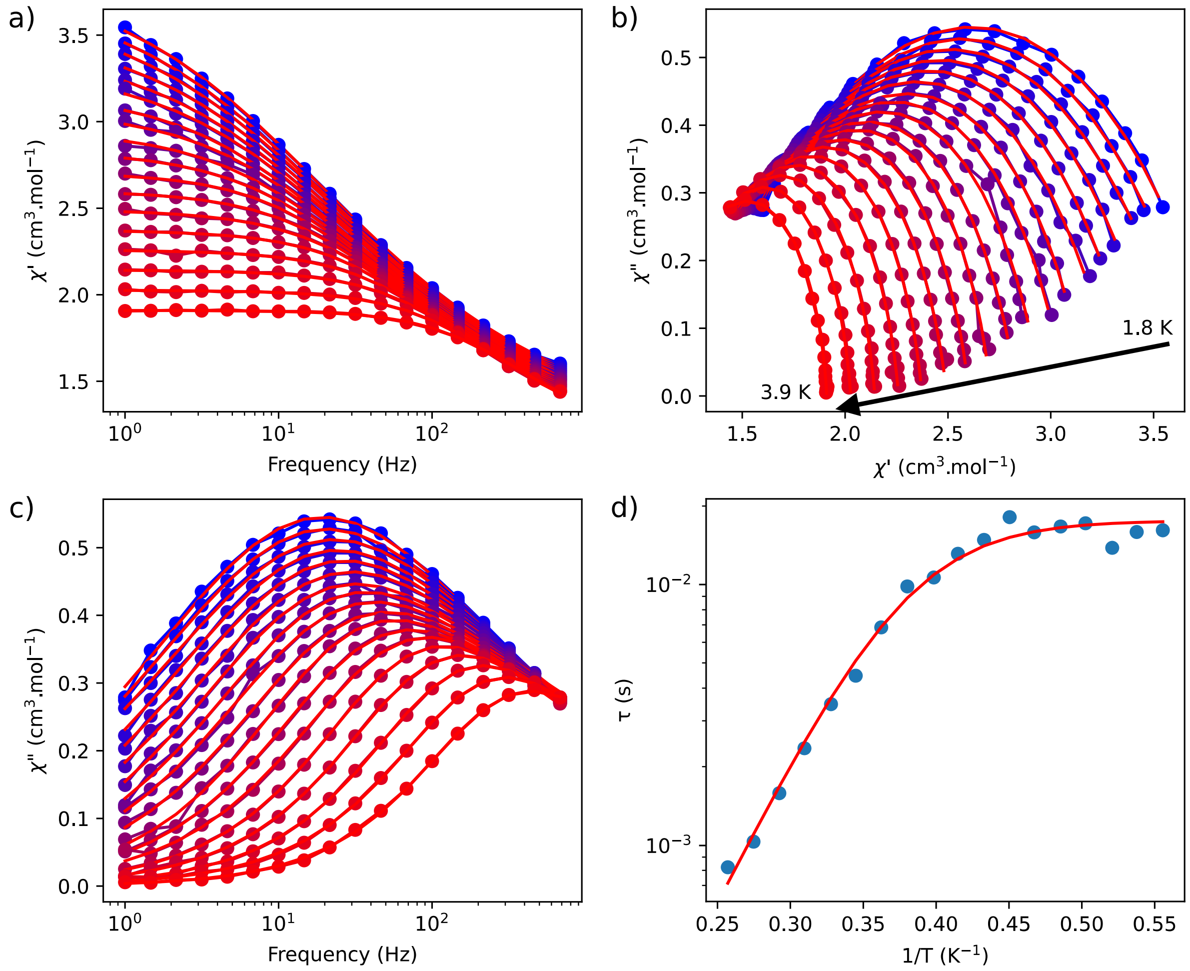

Figure S8. Frequency dependence of the in-phase, χ', (a) and out-of-phase, χ'' (c) components of the ac susceptibility for **2** under applied magnetic field of 1000 Oe. The red lines are the result of the Cole-Cole fitting. (b) Cole-Cole plots obtained using the frequency dependence of χ'' for **2** obtained under 1000 Oe. The solid lines correspond to the best fit obtained with a generalized Debye model. (d) Temperature dependence of the relaxation time for **2** (1000 Oe) and the corresponding fit with eq. (2) (red solid line).

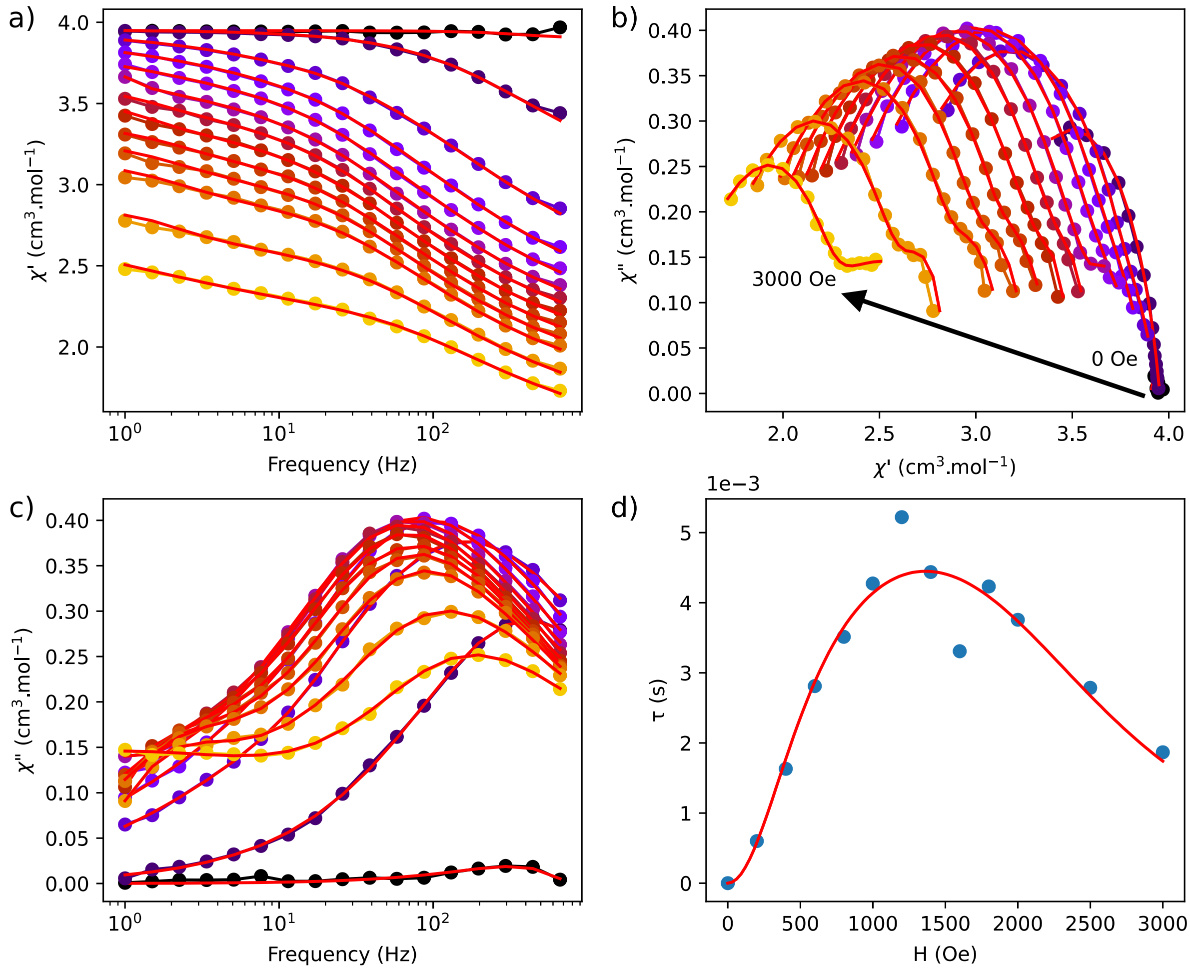

Figure S9. Frequency dependence of χ' (a) and χ'' (c) for **3** at 1.8 K performed under various applied dc fields. (b) Cole-Cole plots obtained using the frequency dependence of χ'' for **3** at 1.8 K under various dc field. The solid lines correspond to the best fit obtained with a generalized Debye model. (d) Field dependence of the relaxation time curve for **3** for the lowest relaxation time. The red line represents the fit using equation (1).

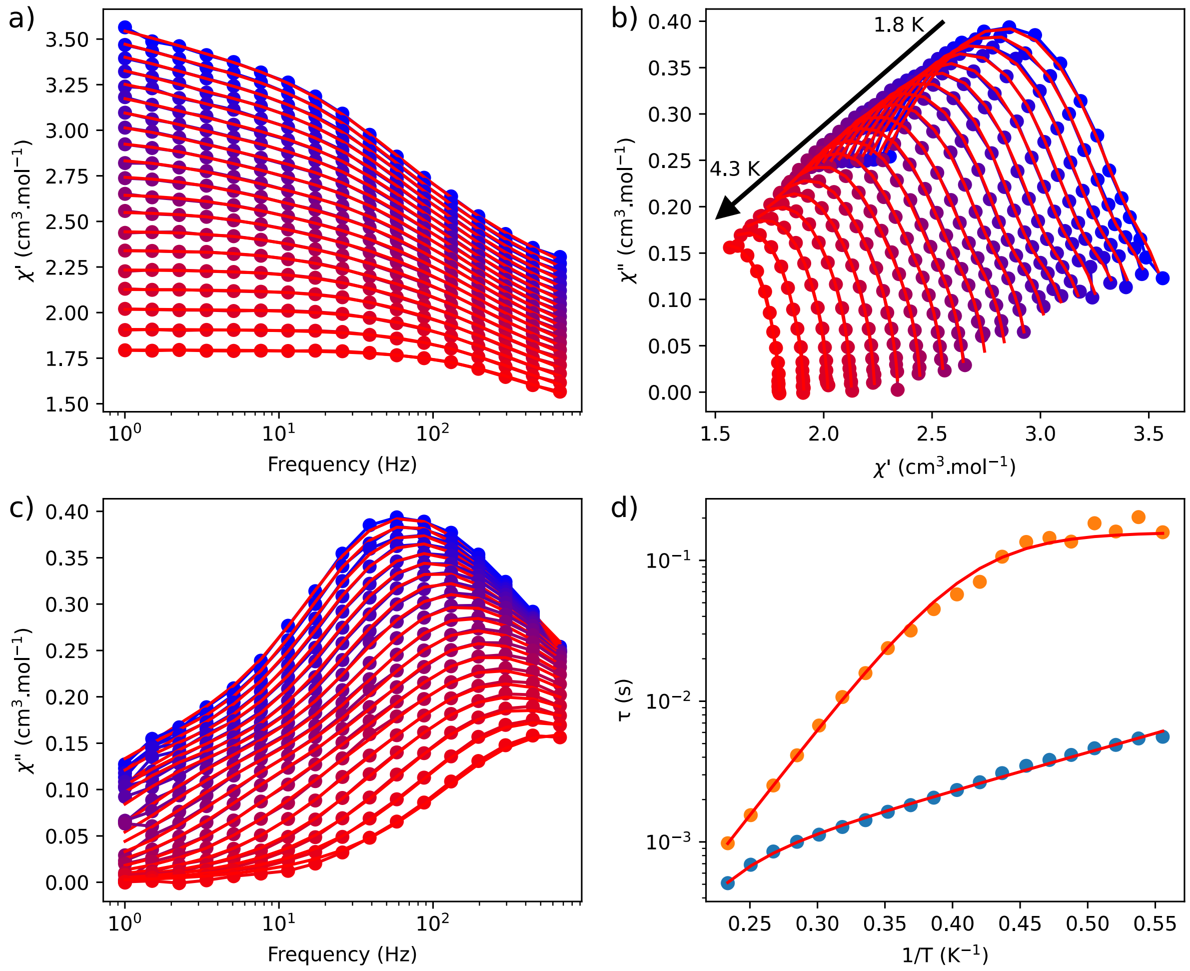

Figure S10. Frequency dependence of the in-phase, χ', (a) and out-of-phase, χ'' (c) components of the ac susceptibility for **3** under applied magnetic field of 1200 Oe. The red lines are the result of the Cole-Cole fitting. (b) Cole-Cole plots obtained using the frequency dependence of χ'' for **3** obtained under 1000 Oe. The solid lines correspond to the best fit obtained with a generalized Debye model. (d) Temperature dependence of the two relaxation times for **3** (1200 Oe) and the corresponding fit with eq. (2) (red solid line).

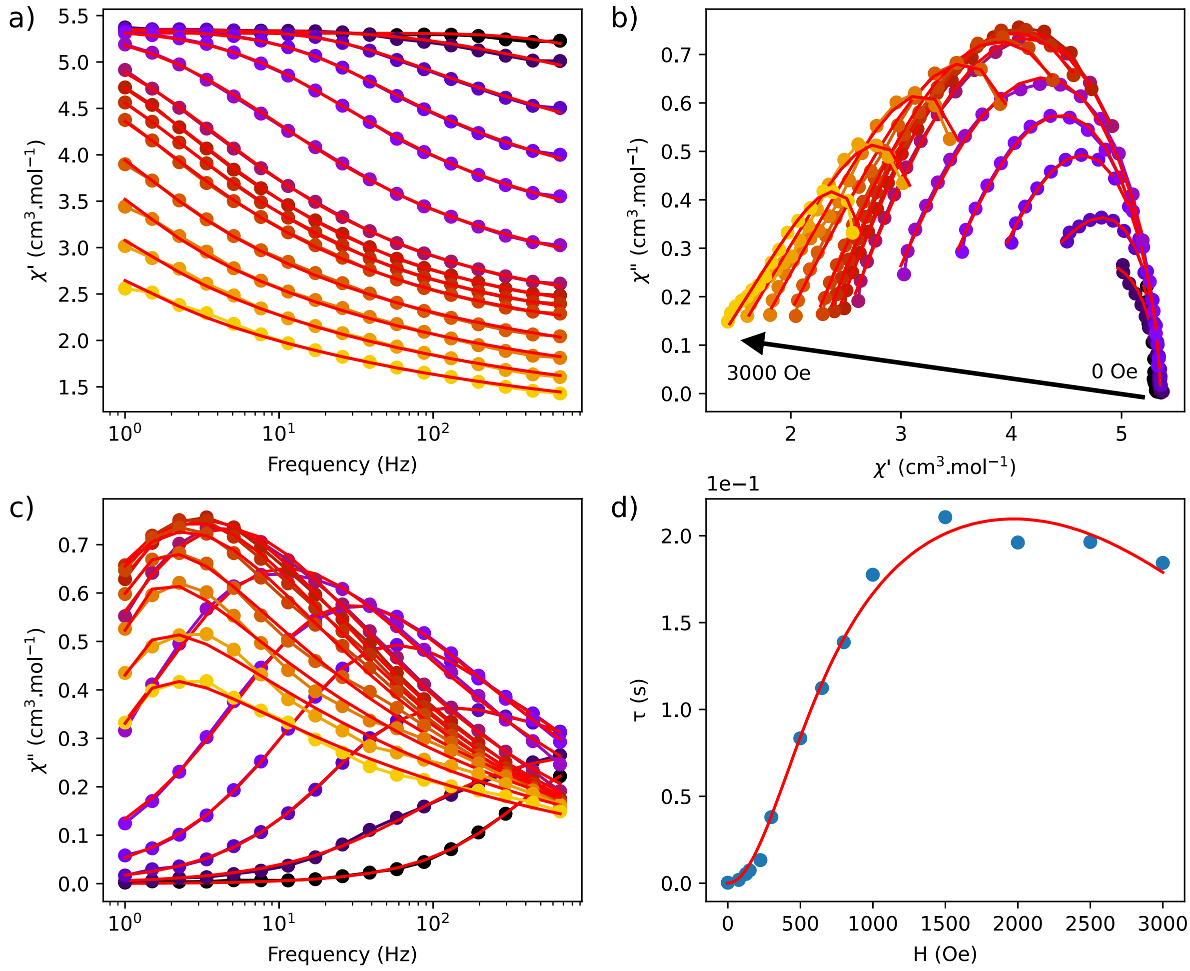

Figure S11. Frequency dependence of χ' (a) and χ'' (c) for **4** at 1.8 K performed under various applied dc fields. (b) Cole-Cole plots obtained using the frequency dependence of χ'' for **4** at 1.8 K under various dc field. The solid lines correspond to the best fit obtained with a generalized Debye model. (d) Field dependence of the relaxation time curve for **4** for the lowest relaxation time. The red line represents the fit using equation (1).

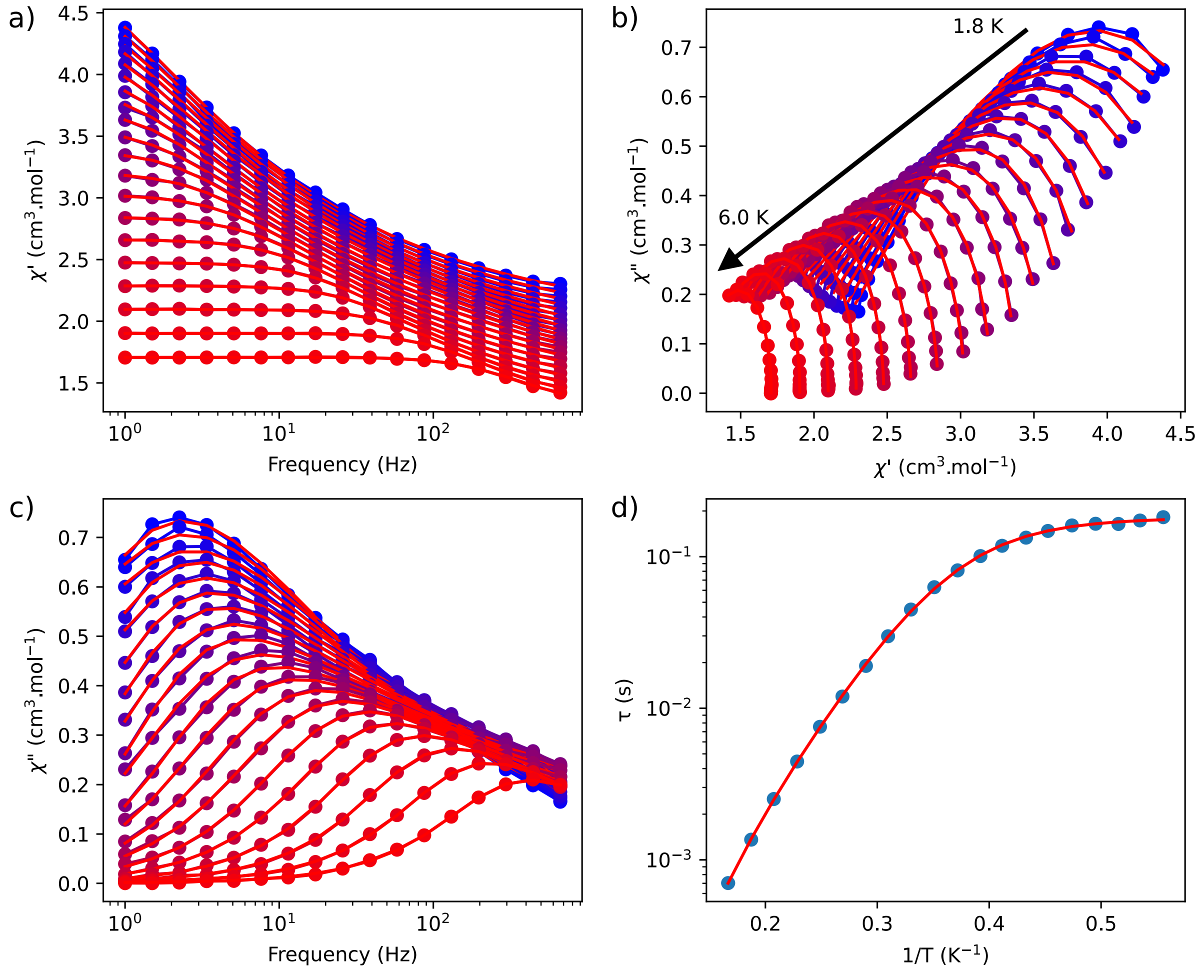

Figure S12. Frequency dependence of the in-phase, χ', (a) and out-of-phase, χ'' (c) components of the ac susceptibility for **4** under applied magnetic field of 1000 Oe. The red lines are the result of the Cole-Cole fitting. (b) Cole-Cole plots obtained using the frequency dependence of χ'' for **4** obtained under 1000 Oe. The solid lines correspond to the best fit obtained with a generalized Debye model. (d) Temperature dependence of the two relaxation times for **4** (1000 Oe) and the corresponding fit with eq. (2) (red solid line).

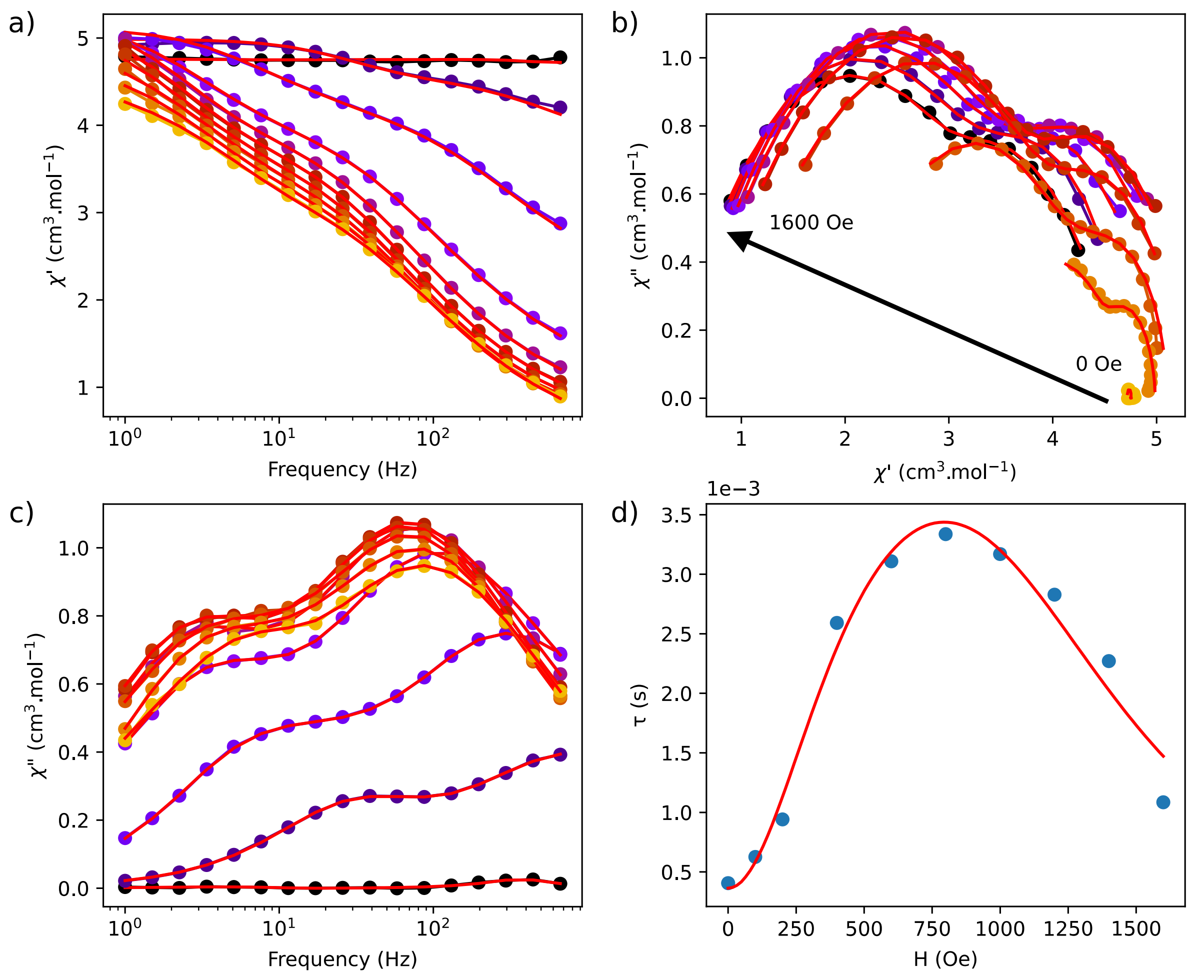

Figure S13. Frequency dependence of χ' (a) and χ'' (c) for **5** at 1.8 K performed under various applied dc fields. (b) Cole-Cole plots obtained using the frequency dependence of χ'' for **5** at 1.8 K under various dc field. The solid lines correspond to the best fit obtained with a generalized Debye model. (d) Field dependence of the relaxation time curve for **5** for the lowest relaxation time. The red line represents the fit using equation (1).

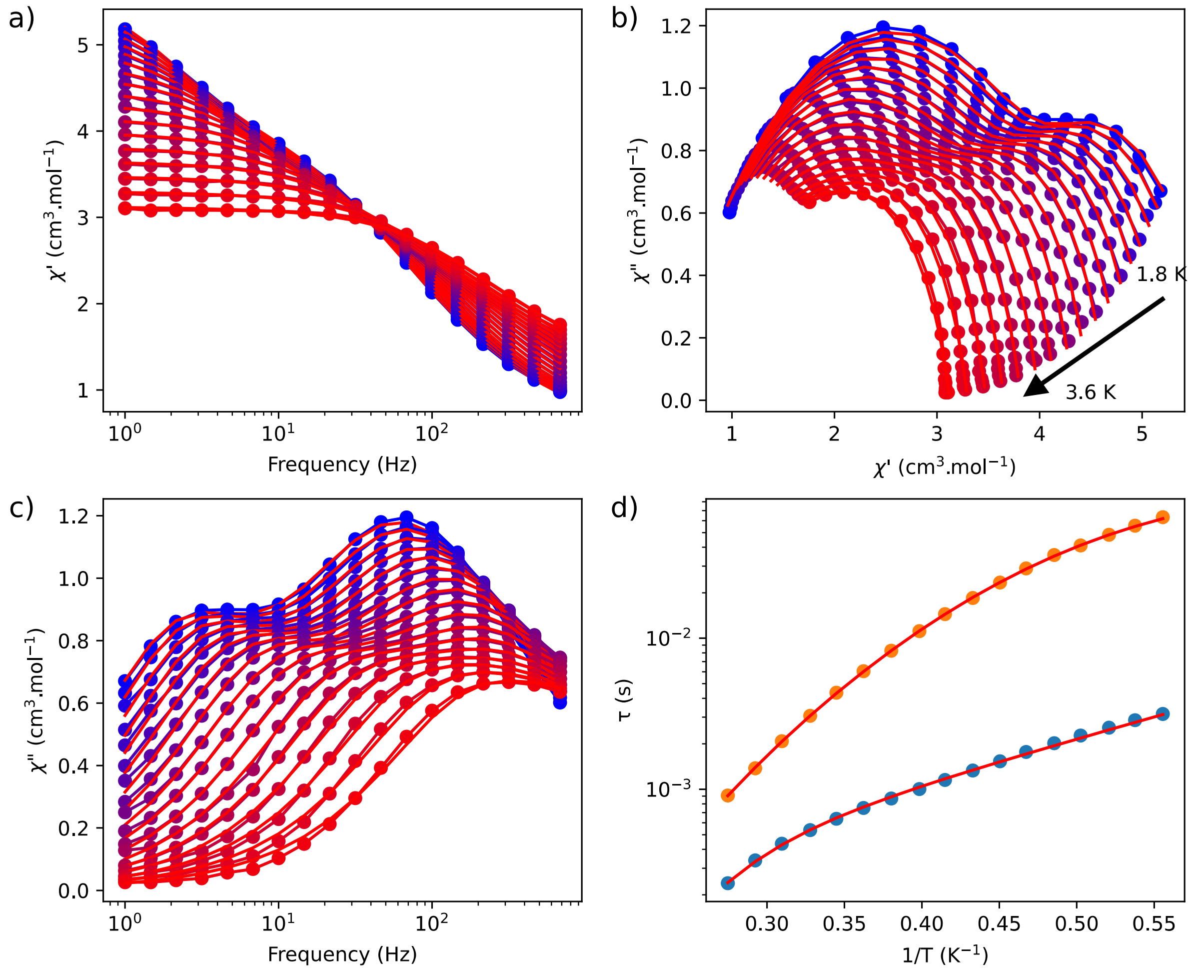

Figure S14. Frequency dependence of the in-phase, χ', (a) and out-of-phase, χ'' (c) components of the ac susceptibility for **5** under applied magnetic field of 1000 Oe. The red lines are the result of the Cole-Cole fitting. (b) Cole-Cole plots obtained using the frequency dependence of χ'' for **5** obtained under 1000 Oe. The solid lines correspond to the best fit obtained with a generalized Debye model. (d) Temperature dependence of the two relaxation times for **5** (1000 Oe) and the corresponding fit with eq. (2) (red solid line).

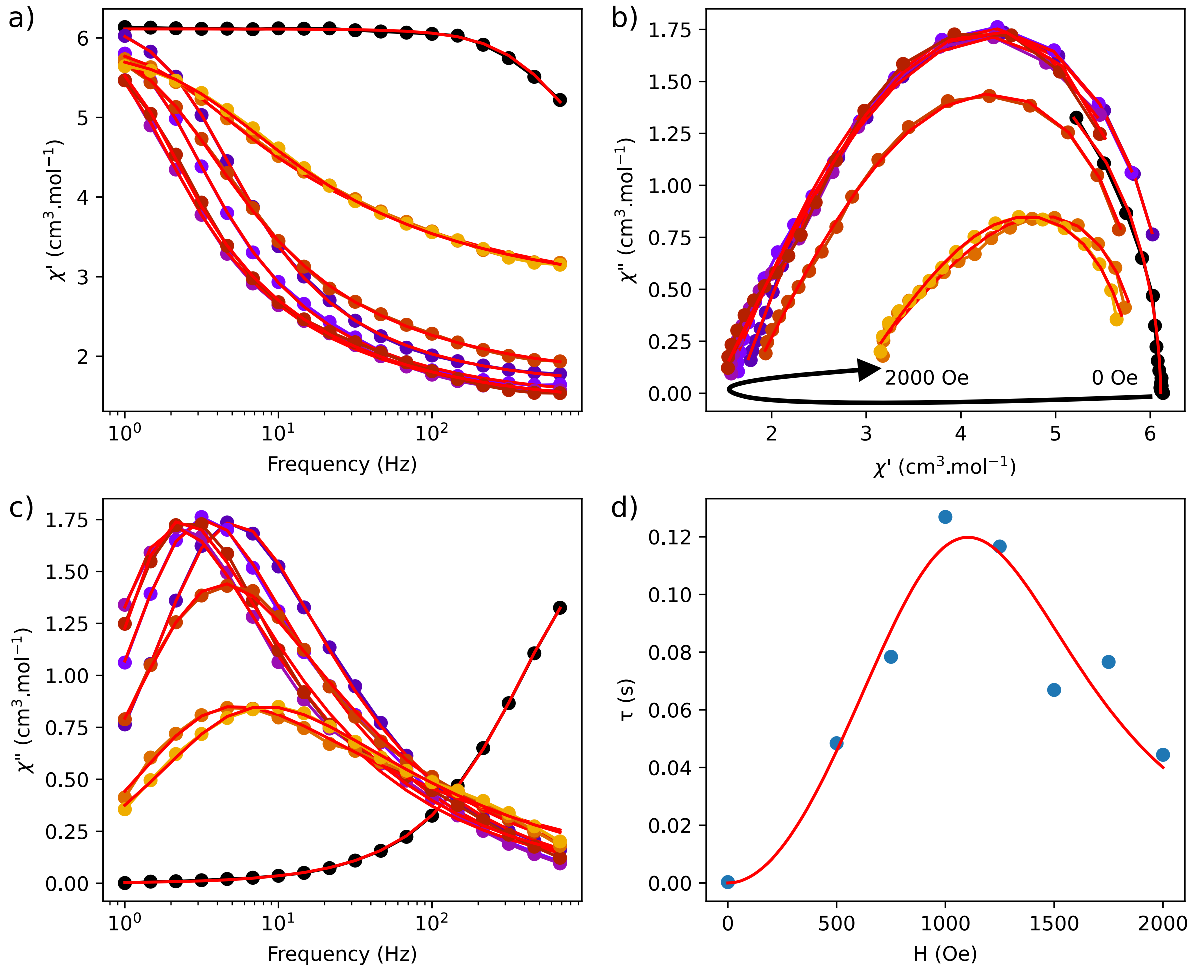

Figure S15. Frequency dependence of χ' (a) and χ'' (c) for **6** at 1.8 K performed under various applied dc fields. (b) Cole-Cole plots obtained using the frequency dependence of χ'' for **6** at 1.8 K under various dc field. The solid lines correspond to the best fit obtained with a generalized Debye model. (d) Field dependence of the relaxation time curve for **6** for the lowest relaxation time. The red line represents the fit using equation (1).

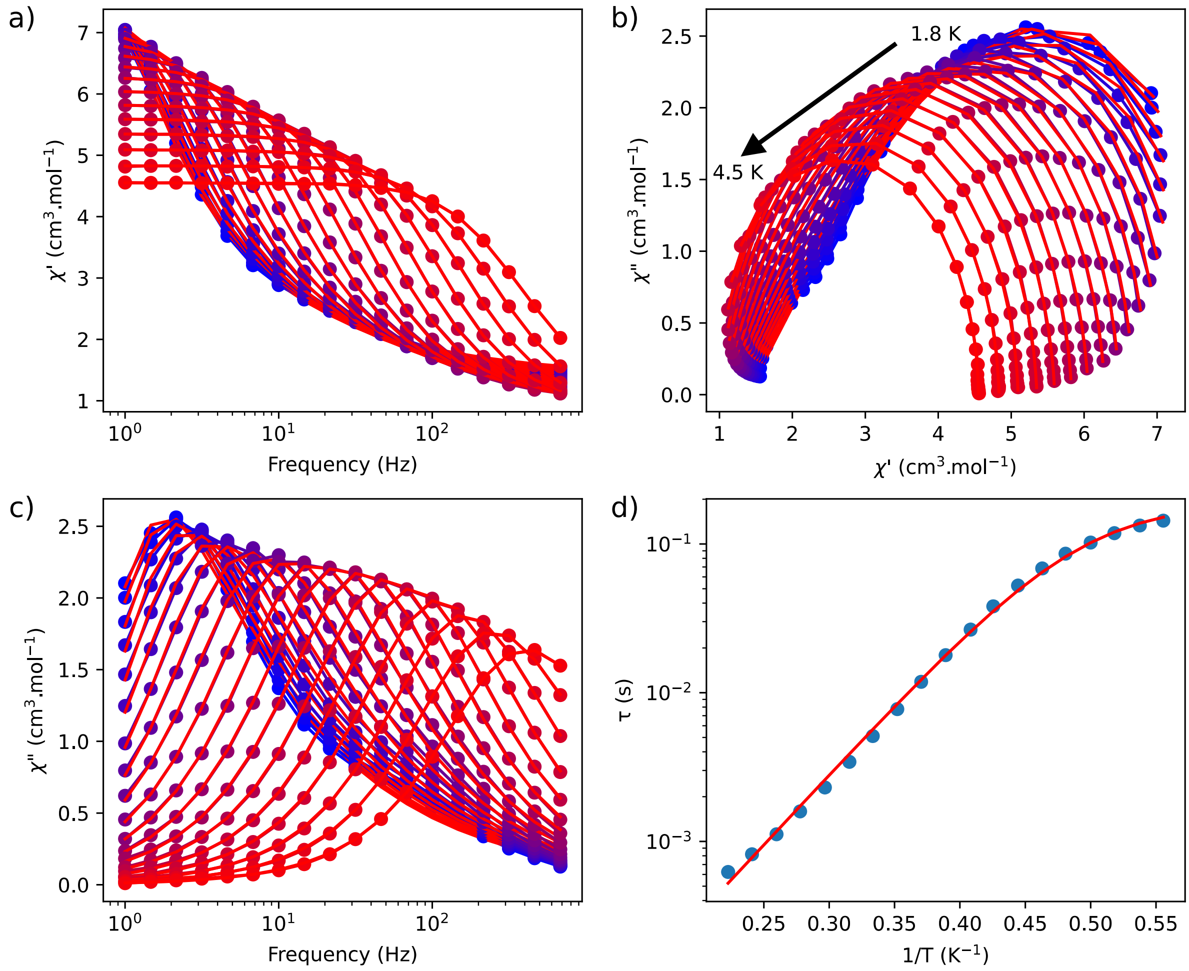

Figure S16. Frequency dependence of the in-phase, χ', (a) and out-of-phase, χ'' (c) components of the ac susceptibility for **6** under applied magnetic field of 1000 Oe. The red lines are the result of the Cole-Cole fitting. (b) Cole-Cole plots obtained using the frequency dependence of χ'' for **6** obtained under 1000 Oe. The solid lines correspond to the best fit obtained with a generalized Debye model. (d) Temperature dependence of the two relaxation times for **6** (1000 Oe) and the corresponding fit with eq. (2) (red solid line).

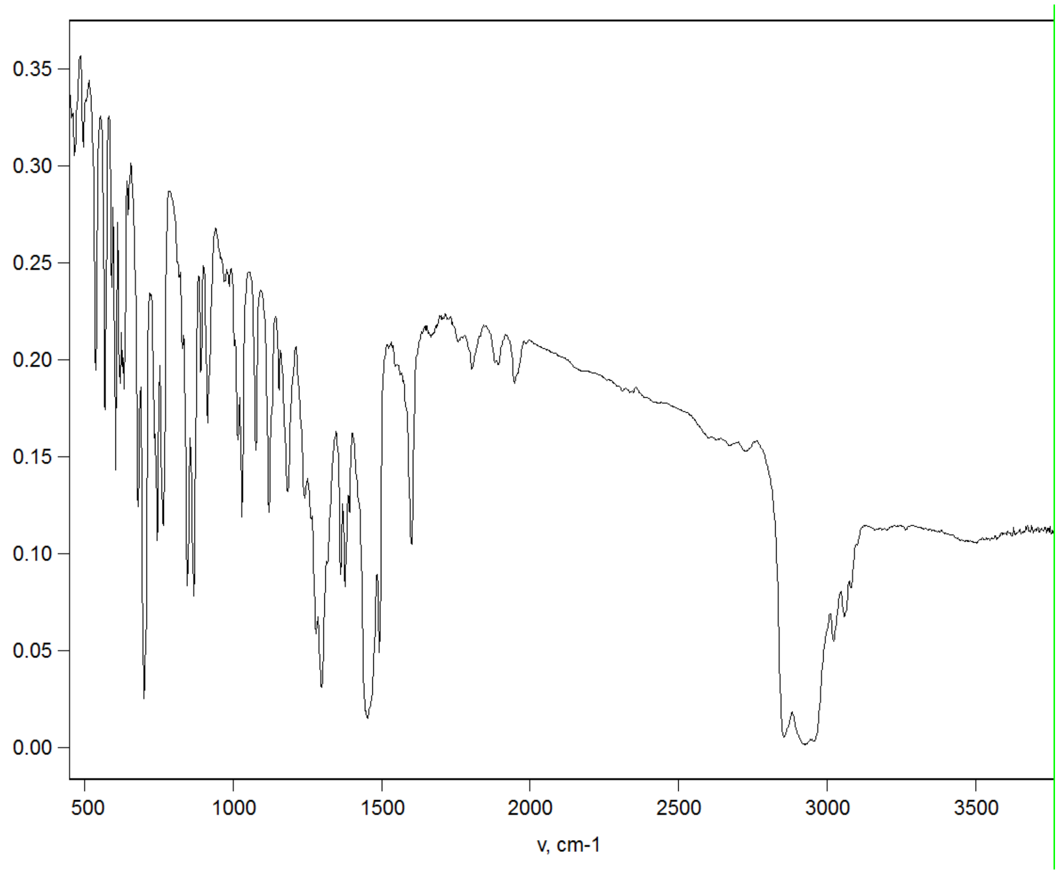

Figure S17. IR spectrum of [4-tBuC$_6$H$_2$(2,6-benzhydryl)O]$_3$Er(THF) **1**.

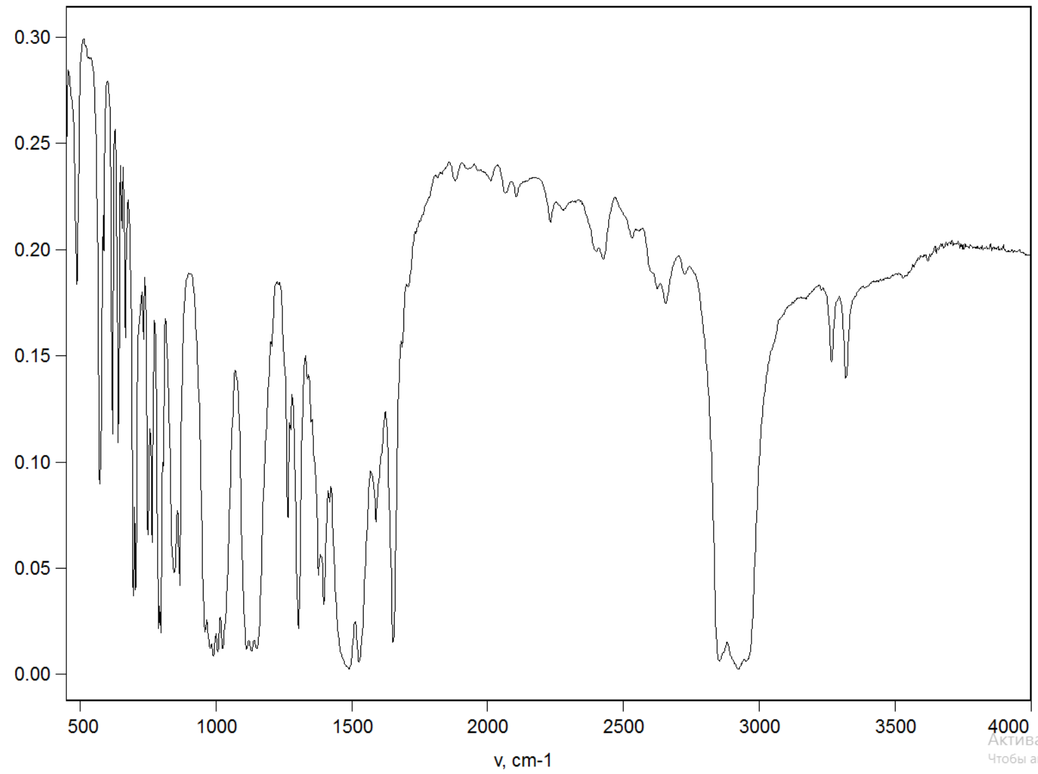

Figure S18. IR spectrum of [(C$_6$F$_5$)$_3$CO]$_3$Er(Me$_3$SiOH) **2**.

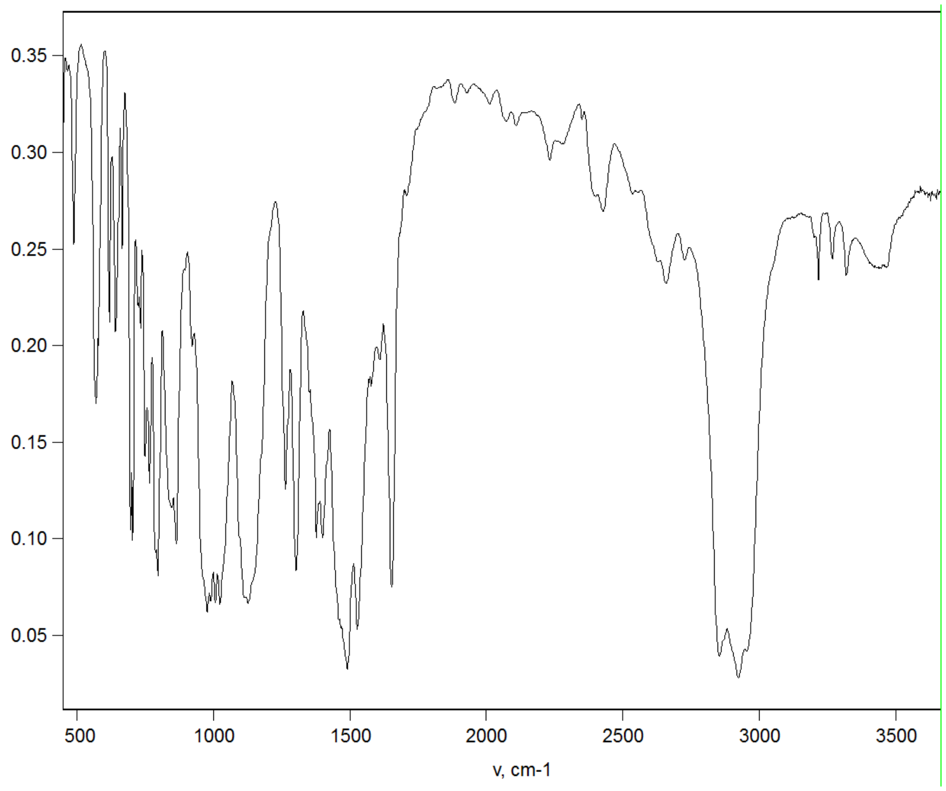

Figure S19. IR spectrum of $[(C_6F_5)_3CO]_3Er((Me_3Si)_2NH)$ **3**.

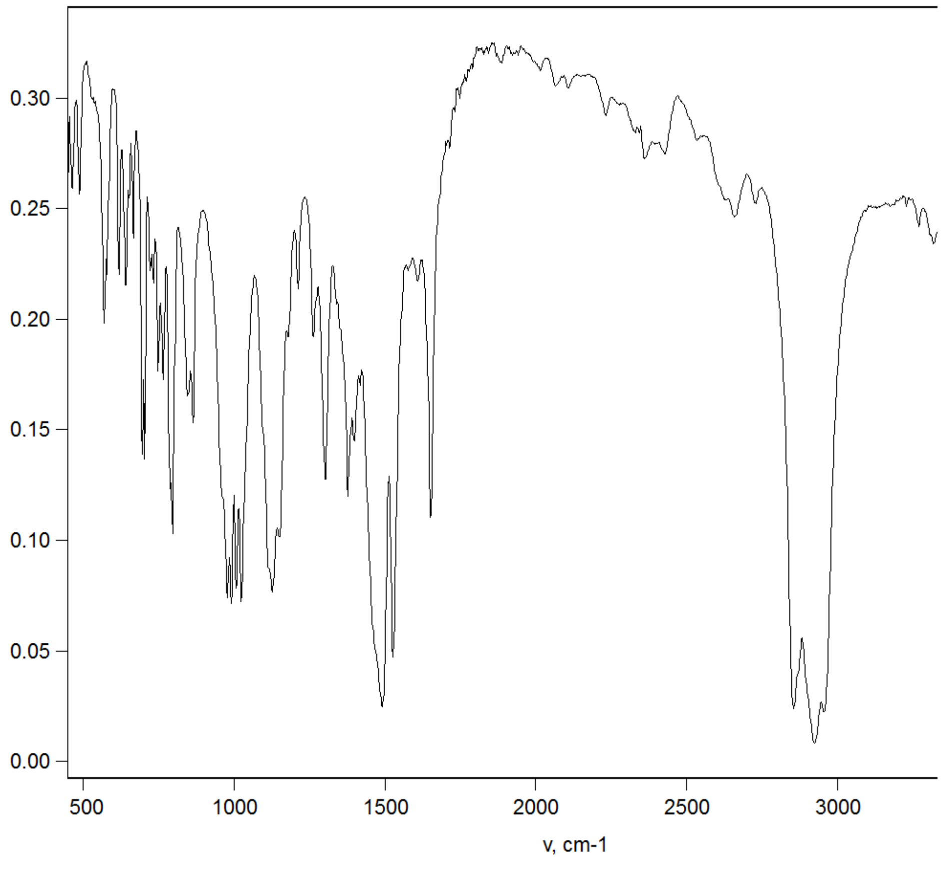

Figure S20. IR spectrum of $[(C_6F_5)_3CO]_3Er(C_6H_5CH_3)$ **4**.

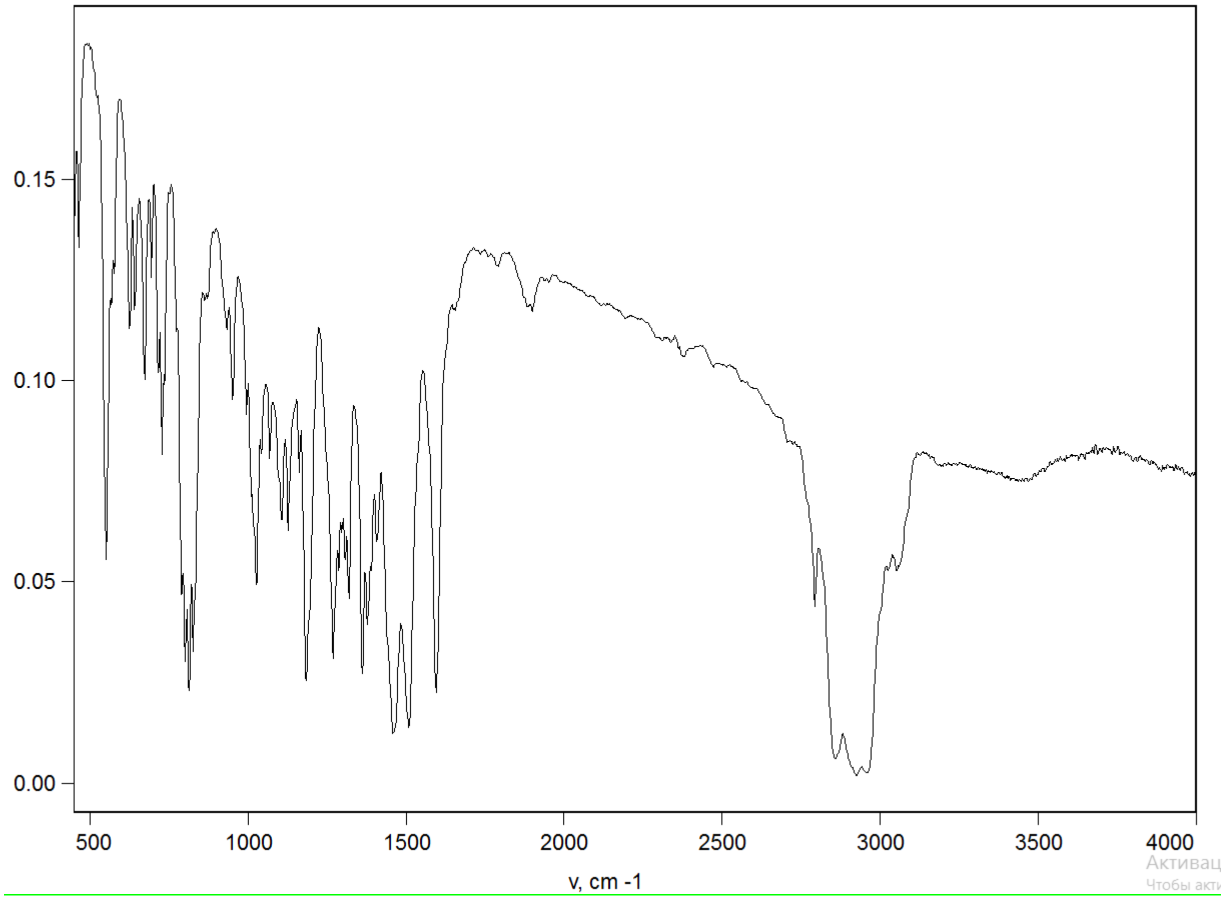

Figure S21. IR spectrum of $[(C_6F_5)_3CO]_3Er(o\text{-}Me_2NC_6H_4CH_3)$ **5**.

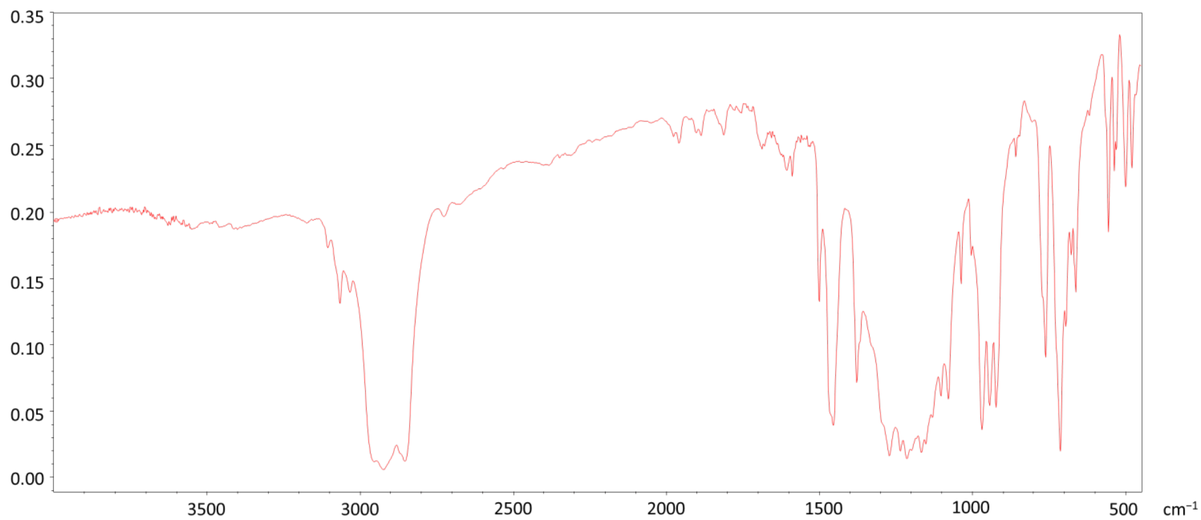

Figure S22. IR spectrum of $\{[Ph(F_3C)_2CO]_2Er(\mu\text{-}OC(CF_3)_2Ph]\}_2$ **6**.

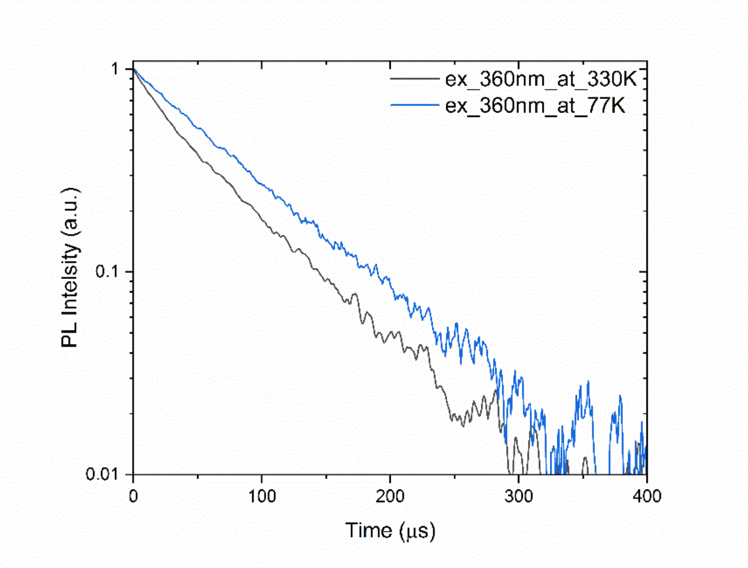

Figure S23. Luminescence kinetics of complex **4** in solid phase at temperatures of 77 and 300 K under optical excitation through ligand environment (360 nm). Recording wavelength is 1535 nm.

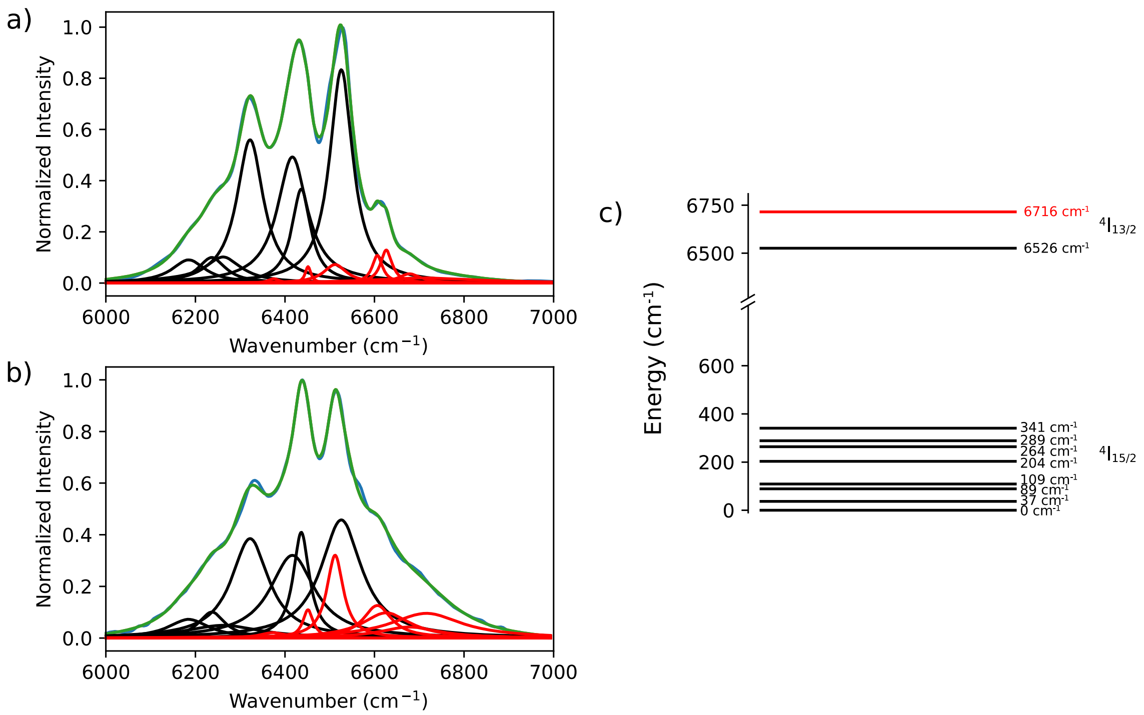

Figure S24. Experimental luminescence emission spectra for crystalline complexes **2** at 77 K (a) and 300 K (b). The blue and green curves represent the experimental data and the optimized fit. The black and red Lorentzian functions represent the radiative relaxation from the first and second $^4I_{13/2}$ states, respectively. c) Schematic representation of the energy levels for sample **2**, extracted from the fitting process.

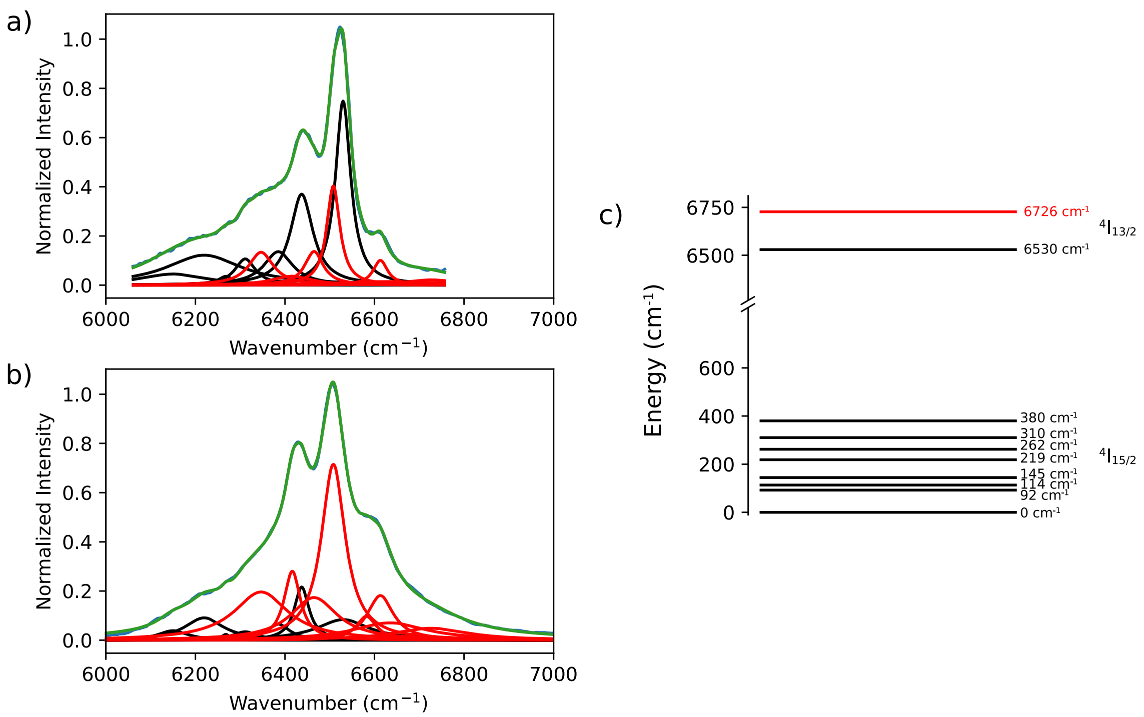

Figure S25. Experimental luminescence emission spectra for crystalline complexes **3** at 77 K (a) and 300 K (b). The blue and green curves represent the experimental data and the optimized fit. The black and red Lorentzian functions represent the radiative relaxation from the first and second $^4I_{13/2}$ states, respectively. c) Schematic representation of the energy levels for sample **3**, extracted from the fitting process.

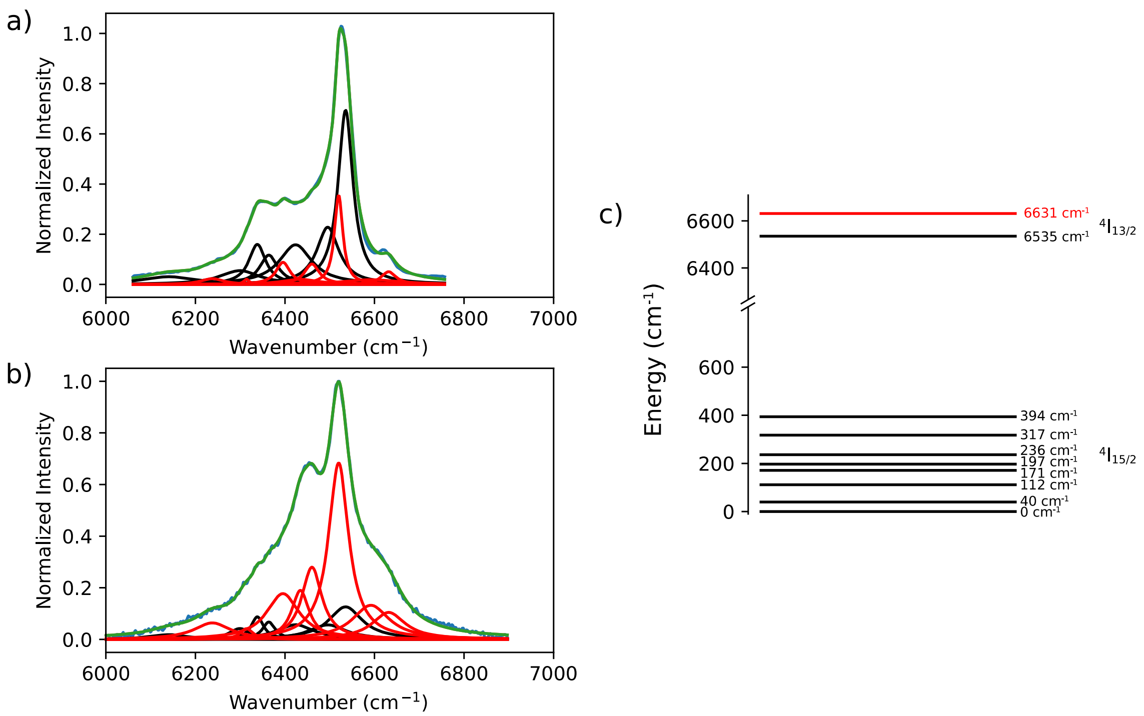

Figure S26. Experimental luminescence emission spectra for crystalline complexes **4** at 77 K (a) and 300 K (b). The blue and green curves represent the experimental data and the optimized fit. The black and red Lorentzian functions represent the radiative relaxation from the first and second $^4I_{13/2}$ states, respectively. c) Schematic representation of the energy levels for sample **4**, extracted from the fitting process.

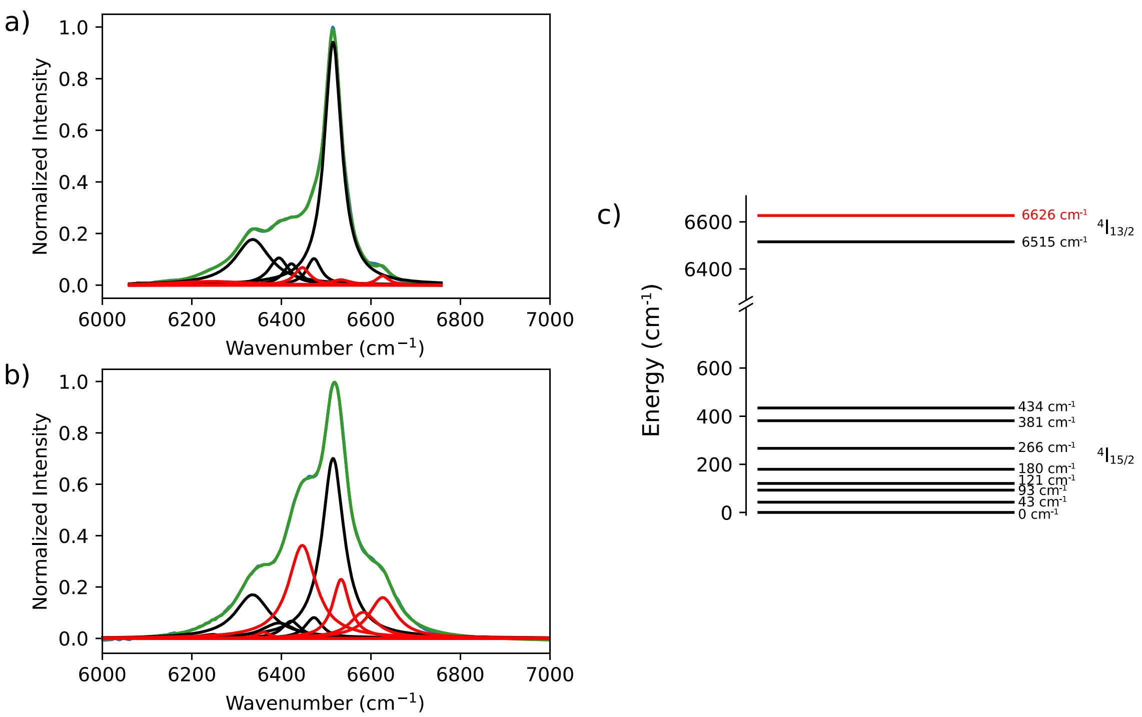

Figure S27. Experimental luminescence emission spectra for crystalline complexes **5** at 77 K (a) and 300 K (b). The blue and green curves represent the experimental data and the optimized fit. The black and red Lorentzian functions represent the radiative relaxation from the first and second $^4I_{13/2}$ states, respectively. c) Schematic representation of the energy levels for sample **5**, extracted from the fitting process.

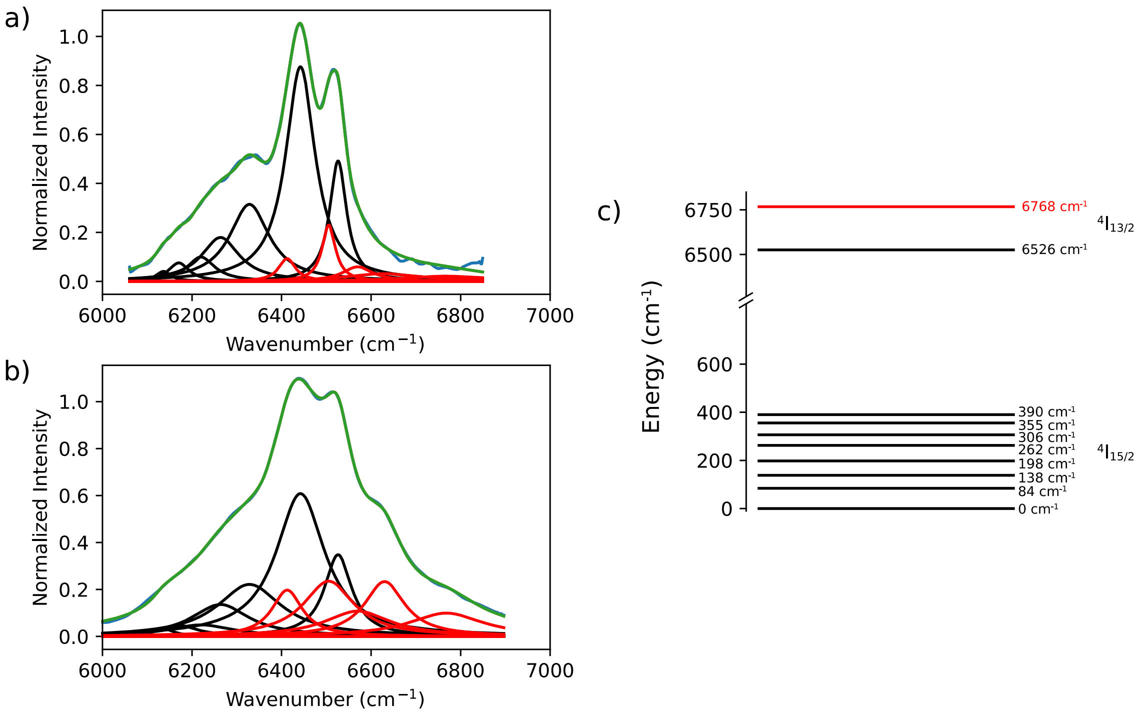

Figure S28. Experimental luminescence emission spectra for crystalline complexes **6** at 77 K (a) and 300 K (b). The blue and green curves represent the experimental data and the optimized fit. The black and red Lorentzian functions represent the radiative relaxation from the first and second $^4I_{13/2}$ states, respectively. c) Schematic representation of the energy levels for sample **6**, extracted from the fitting process.

Table S1: Representative examples of Er^{3+} luminescent SMMs.

Compounds	Magnetism	Luminescence	Ref.
[Er(thd)$_3$(bath)] 8-coordinated Er^{3+}	Field induced SMM, two relaxations: U_{eff}= 15.6 and 22.4 K.	RT NIR emission, λ_{ex}=337 nm (antenna effect), λ_{em}=1532 nm, associated with the $^4I_{13/2}\rightarrow{}^4I_{15/2}$ transition	1
8-coordinated Er^{3+} [Er(h)$_3$(bipy)] [Er(h)$_3$(5NO$_2$phen)] [Er(h)$_3$(bath)]	Field induced SMMs, U_{eff}=7.98 K U_{eff}=12.97 K U_{eff}=22.81 K	RT NIR emission, λ_{ex}=405 nm (antenna effect), λ_{em}~1532 nm, associated with the $^4I_{13/2}\rightarrow{}^4I_{15/2}$ transition	2
[Er(notpH$_4$)(H$_2$O)]ClO$_4$·3H$_2$O 2D layered coordination polymer	Field induced SMM, U_{eff}=24 cm^{-1} Correlation with luminescence thanks to the presence of hot bands (emission from $^4I_{13/2}$ multiplet) → energy diagram of the Stark-sub-levels	RT NIR emission, λ_{ex} = 1064 nm (direct Er^{3+} excitation), λ_{em}~1532 nm. The luminescence permitted to establish the energy diagram and determine the energy gap between the ground and first excited state of the $^4I_{15/2}$ CF splitting of 31.2 cm^{-1}, close to the U_{eff} of 24.2 cm^{-1}.	3
[Er(dbm)$_3$(bipy)] 8-coordinated Er^{3+}	Field induced SMM, U_{eff} =19.8 K.	RT NIR emission, λ_{ex}=380 nm (antenna effect), λ_{em}=1532 nm, associated to the $^4I_{13/2}\rightarrow{}^4I_{15/2}$ transition; life time 1.1 μs	4
[ErL$^1_3$]·CH$_3$OH [ErL$^1_2$(tmh)(CH$_3$OH)]·Solv [ErL$^1_2$(tta)(CH$_3$OH)]·CH$_3$OH 8-coordinated Er^{3+}	Field induced SMM, U_{eff}=16.0 K U_{eff}=30.4 K U_{eff}=25.8 K.	RT NIR emission, λ_{ex}=355 nm (antenna effect), λ_{em}=1530 nm, associated to the $^4I_{13/2}\rightarrow{}^4I_{15/2}$ transition; life time 2.37 μs.	5
[Er(depma)$_2$(H$_2$O)$_6$]Cl$_3$)]·Solv	Field induced SMM, U_{eff}=9.8 K	λ_{ex}=330 nm, RT visible emission from anthracene λ_{em}=450 nm.	6
(nBu$_4$N)$_2$[Er(NO$_3$)$_5$] 10-coordinated Er^{3+}	Field induced SMM, U_{eff}=22.3 K	Very low RT NIR emission, at 1550 nm associated to the $^4I_{13/2}\rightarrow{}^4I_{15/2}$ transition	7
8-coordinated Er^{3+} [Er(tpm)$_3$(bipy)] [Er(tfa)$_3$(bipy)]	Genuine SMM U_{eff} =21 K (zero DC applied field) Field induced SMM U_{eff}=15 K	RT NIR emission, λ_{ex}=337 or 532 nm (antenna effect), λ_{em}=1532 nm, associated to the $^4I_{13/2}\rightarrow{}^4I_{15/2}$ transition; life time 1.24 μs	8
Coordination polymers [Er{Ir(ppy)$_2$(dcbpy)}$_2$(NO$_3$) (H$_2$O)$_n$] [Er$_2$(OH){Ir(ppy)$_2$(dcbpy)}$_4$(NO$_3$)(HO)$_4$]	Field induced SMM, U_{eff}=13.6 K U_{eff}=11.8 K	Emission at 584 nm from Ir unit (λ_{ex}=375 nm) and at 1538 nm (λ_{ex}= 500 nm); life time 1.4 μs (λ_{ex}=500 nm)	9
3D neutral polymorphic frameworks [Er$_2$(trz$_2$An)$_3$(H$_2$O)$_4$]$_n$·H$_2$O	Field induced SMM, U_{eff}=42 K	NIR emission at 77K and RT, λ_{ex}=355 nm (antenna effect), emission associated to the Er^{3+}	10

		$^4I_{13/2}\rightarrow{}^4I_{15/2}$ transition; life time of 55 ns and 86 ns	
$(Et_3NH)[Er(L^2)_2]\cdot1.5H_2O$ $[Zn(\mu\text{-}L^3)(\mu\text{-}NO_3)Er(NO_3)_2]$	Field induced SMM, U_{eff}=8 K, U_{eff}=15 cm^{-1}	NIR emission at RT, λ_{ex}=380-649 nm (antenna effect), λ_{em}=1550 nm associated to the $^4I_{13/2}\rightarrow{}^4I_{15/2}$ transition.	11
$[Zn(\mu\text{-}L^3)(\mu\text{-}OAc)Er(NO_3)_2]$	Field induced SMM, U_{eff}=8 cm^{-1}	NIR emission at RT, λ_{ex}=355 nm, λ_{em}=1530 nm associated to the $^4I_{13/2}\rightarrow{}^4I_{15/2}$ transition; life time 2.77 μs, 11.82 μs	12
$[Er(hfac)_3(tempo)_2]$	Field induced SMM, U_{eff}=12 cm^{-1}	NIR emission at 4.2K, λ_{em} associated to the $^4I_{13/2}\rightarrow{}^4I_{15/2}$ transition; life time 11.82 μs.	13

thd = 2,2,6,6-tetramethyl-3,5-heptanedionate, bath = bathophenanthroline; h = 2,4-hexanedionate; bipy = 2,2-bipyridine; 5NO2phen = 5-nitro-1,10-phenanthroline; bath = bathophenanthroline; $notpH_4^{2-}$ = = 1,4,7-triazacyclononane-1,4,7-triyl-tris(methylenephosphonate); dbm = dibenzoylmethanate; HL^1=2-(tetrazol-5-yl)-1,10-phenanthroline; tmh = 2,2,6,6-tetramethylheptanoate; tta = thenoyltrifluoroacetonate; ppy = 2-phenylpyridine; dcbpy = 2,2′-bipyridine-4,4′-dicarboxylate; depma = 9–diethylphosphono–methylanthracene; Htpm =1,1,1-trifluoro-5,5-dimethyl-2,4-hexanedione; Htfa = 4,4,4-trifluoro-1-(2-furyl)-1,3-butanedione); SYML=(N,N0-bis(1-naphthaldiamine)-O-phenylenediamine); H_2trz_2An = 3,6-N-ditriazolyl-2,5-dihydroxy-1,4-benzoquinone. L^2 = ***N*,*N′***-bis(3-nitro-salicylaldehyde)ethylenediamine dianion); H_2L^3 = *N,N′,N″*-trimethyl-*N,N″*-bis(2-hydroxy-3-methoxy-5-methylbenzyl)diethylenetriamine ; TEMPO = (2,2,6,6-tetramethylpiperidin-1-oxyl) radical.

Table S2: Crystal data, data collection and structure refinement details for **1-6**.

	1	**2**	**3**	**4**	**5**	**6**
Formula	$C_{122.5}H_{119}ErO_4$	$C_{60}H_{10}ErF_{45}O_4Si$	$C_{63}H_{19}ErF_{45}NO_3Si_2$	$C_{64}H_8ErF_{45}O_3$	$C_{66}H_{13}ErF_{45}NO_3$	$C_{54}H_{30}Er_2F_{36}O_6$
M	1822.43	1845.03	1916.23	1846.96	1890.03	1793.30
T, K	100.0(2)	100.0(2)	100.0(2)	100.0(2)	100.0(2)	100.0(2)
Crystal system	Triclinic	Trigonal	Triclinic	Triclinic	Triclinic	Triclinic
Space group	*P-1*	*R-3*	*P-1*	*P-1*	*P-1*	*P-1*
a, Å	13.02470(10)	17.2887(3)	14.7886(4)	13.5916(6)	15.0250(4)	11.2800(2)
b, Å	14.11930(10)	17.2887(3)	15.4929(4)	15.0450(5)	15.1826(4)	13.6848(3)
c, Å	27.7895(2)	35.2684(5)	18.0735(4)	18.6919(8)	15.5060(4)	20.1615(5)
α, deg	84.4770(10)	90	94.9370(10)	73.966(3)	84.4720(10)	100.9240(10)
β, deg	83.5680(10)	90	112.0700(10)	79.560(3)	83.219(2)	104.5260(10)
γ, deg	72.6830(10)	120	96.0260(10)	64.614(2)	83.909(2)	94.4460(10)
V, Å^3	4837.46(7)	9129.4(3)	3780.78(17)	3310.1(2)	3480.03(16)	2932.43(11)
Z	2	6	2	2	2	2
d_{calc}, g/cm$_3$	1.251	2.014	1.683	1.853	1.804	2.031
μ, mm^{-1}	0.923	1.587	1.296	1.441	1.374	3.007
F_{000}	1908	5334	1858	1778	1826	1724
Crystal dimensions, mm	0.62×0.50×0.34	0.15×0.10×0.10	0.15×0.10×0.05	0.25×0.25×0.02	0.25×0.20×0.03	0.25×0.20×0.03
θ range for data collection, deg	1.74–30.03	2.36–27.00	1.86–27.00	1.82–26.00	1.80–27.00	1.88–27.00
Completeness, %	99.9	99.9	99.7	96.5	99.7	99.8
HKL indices	$-18 \le h \le 18$	$-22 \le h \le 22$	$-18 \le h \le 18$	$-10 \le h \le 16$	$-19 \le h \le 19$	$-14 \le h \le 14$
	$-19 \le k \le 19$	$-18 \le k \le 22$	$-17 \le k \le 19$	$-18 \le k \le 18$	$-19 \le k \le 19$	$-17 \le k \le 17$
	$-39 \le l \le 39$	$-45 \le l \le 45$	$-23 \le l \le 23$	$-22 \le l \le 23$	$-18 \le l \le 19$	$-25 \le l \le 22$
Reflns. collected	170147	34659	42913	23913	37911	32777
Reflns. unique ($I > 2\sigma(I)$)	26368	4092	12863	6906	12837	11020
R_{int}	0.0468	0.0320	0.0597	0.0843	0.0385	0.0355

Data / restraints / parameters	28285 / 1109 / 1199	4433 / 13 / 346	16441 / 0 / 1042	12557 / 30 / 1021	15149 / 56 / 1058	12801 / 0 / 883
$S(F^2)$	1.044	1.079	0.996	0.958	1.020	1.061
R_1 / wR_2 ($I > 2\sigma(I)$)	0.0320 / 0.0724	0.0324 / 0.0899	0.0477 / 0.1051	0.0725 / 0.1473	0.0427 / 0.0995	0.0304 / 0.0678
R_1 / wR_2 (all data)	0.0360 / 0.0740	0.0363 / 0.0935	0.0663 / 0.1125	0.1312 / 0.1673	0.0528 / 0.1044	0.0382 / 0.0710
Largest diff. peak and hole, e/Å^3	0.86 / −1.31	0.94 / −1.33	1.49 / −0.86	1.42 / −1.35	1.34 / −0.75	1.40 / −1.10

Table S3. Main magnetic parameters utilized in Equation (1) for samples **1–6**.

Complex	D ($s^{-1}.Oe^{-4}.K^{-1}$)	B_1 (s^{-1})	B_2 (Oe^{-2})	C (s^{-1})
		B_0 ($s^{-1}.Oe^{-2}$)		
1	$(1.6 \pm 0.1)\ 10^{-11}$	$10^{(4.2 \pm 0.9)}$	$10^{(-2.9 \pm 0.9)}$	300 ± 7
2	$(5.4 \pm 1.0)\ 10^{-11}$	$10^{(4.1 \pm 1.0)}$	$10^{(-3.0 \pm 1.5)}$	150 ± 17
3	$(2.7 \pm 0.7)\ 10^{-12}$	$(6.2 \pm 1.5)\ 10^{7}$		174 ± 18
4	$(9.3 \pm 2.0)\ 10^{-15}$	$(2.0 \pm 0.2)\ 10^{6}$		4.0 ± 0.2
5	$(3.9 \pm 0.7)\ 10^{-11}$	$10^{(3.4 \pm 0.2)}$	$10^{(-4.1 \pm 0.3)}$	206 ± 28
6	$(7.4 \pm 2.1)\ 10^{-13}$	$(4.8 \pm 1.6)\ 10^{6}$		2.4 ± 2.1

References

1 P. Martín-Ramos, M. Ramos Silva, J. T. Coutinho, L. C. J. Pereira, P. Chamorro-Posada and J. Martín-Gil, *European Journal of Inorganic Chemistry*, 2014, **2014**, 511–517.
2 M. R. Silva, P. Martín-Ramos, J. T. Coutinho, L. C. J. Pereira and J. Martín-Gil, *Dalton Trans.*, 2014, **43**, 6752–6761.
3 M. Ren, S.-S. Bao, R. A. S. Ferreira, L.-M. Zheng and L. D. Carlos, *Chem. Commun.*, 2014, **50**, 7621–7624.
4 P. Martín-Ramos, J. T. Coutinho, M. R. Silva, L. C. J. Pereira, F. Lahoz, P. S. P. da Silva, V. Lavín and J. Martín-Gil, *New J. Chem.*, 2015, **39**, 1703–1713.
5 J.-R. Jiménez, I. F. Díaz-Ortega, E. Ruiz, D. Aravena, S. J. A. Pope, E. Colacio and J. M. Herrera, *Chemistry – A European Journal*, 2016, **22**, 14548–14559.
6 Q. Zou, X.-D. Huang, J.-C. Liu, S.-S. Bao and L.-M. Zheng, *Dalton Trans.*, 2019, **48**, 2735–2740.
7 L. Chen, J. Zhou, A. Yuan and Y. Song, *Dalton Trans.*, 2017, **46**, 15812–15818.
8 M. R. Silva, P. Martín-Ramos, J. T. Coutinho, L. C. J. Pereira, V. Lavín, I. R. Martín, P. S. P. Silva and J. Martín-Gil, *Dalton Trans.*, 2014, **44**, 1264–1272.
9 K. Fan, S.-S. Bao, R. Huo, X.-D. Huang, Y.-J. Liu, Z.-W. Yu, M. Kurmoo and L.-M. Zheng, *Inorg. Chem. Front.*, 2020, **7**, 4580–4592.
10 N. Monni, J. J. Baldoví, V. García-López, M. Oggianu, E. Cadoni, F. Quochi, M. Clemente-León, M. L. Mercuri and E. Coronado, *Chem. Sci.*, 2022, **13**, 7419–7428.
11 M. Ren, Z.-L. Xu, S.-S. Bao, T.-T. Wang, Z.-H. Zheng, R. A. S. Ferreira, L.-M. Zheng and L. D. Carlos, *Dalton Trans.*, 2016, **45**, 2974–2982.
12 M. A. Palacios, S. Titos-Padilla, J. Ruiz, J. M. Herrera, S. J. A. Pope, E. K. Brechin and E. Colacio, *Inorg. Chem.*, 2014, **53**, 1465–1474.
13 M. Karbowiak, C. Rudowicz, T. Nakamura, R. Murakami and T. Ishida, *Chemical Physics Letters*, 2016, **662**, 163–168.